ISSN 2222-5617

МІНІСТЕРСТВО ОСВІТИ І НАУКИ УКРАЇНИ

Вісник Харківського Національного Університету імені В.Н.Каразіна

Серія “Фізика”

Випуск 29

Серія започаткована 1998 р.

Харків 2018

УДК 530.1/539.8

Вісник містить статті, присвячені сучасному стану теоретичних та експериментальних досліджень у галузі фізики
Видання призначене для науковців, викладачів, аспірантів та студентів фізичних спеціальностей вищих навчальних закладів та наукових установ.
Видання є фаховим у галузі фіз.-мат. наук (фізика) наказ МОН України №1328 від 21.12.2015.

Затверджено до друку рішенням Вченої ради Харківського національного університету імені В.Н.Каразіна (протокол №1 від 23 січня 2017 р.)

Адреса редакції:
Україна, 61022, Харків, майдан Свободи, 4, Харківський національний університет імені В.Н. Каразіна, фізичний факультет, 057-707-53-83, ruslan.v.vovk@univer.kharkov.ua
Статті пройшли внутрішнє та зовнішнє рецензування.

Свідоцтво про державну реєстрацію КВ №21573-11473Р від 20.08.2015

UDC 530.1/539.8

Bulletin contains articles on the current state of theoretical and experimental research in the field of physics.
The publication is intended for researchers, teachers and students of physical specialties of higher education and research institutions.
The publication is a professional in the field of physics and mathematics science (Physics) ordered MES of Ukraine #1328 from 12.21.2015.

Approved for publication by the decision of the Academic Council of Kharkiv Karazin National University. (Minutes №1 dated January 23, 2017 p.)

Editorial address:
Svobody Sq. 4, 61022, Kharkiv, Ukraine, V.N. Karazin Kharkiv National University, Department of Physics, 057-707-53-83, ruslan.v.vovk@univer.kharkov.ua
All articles reviewed.
Certificate of registration KB number 21573-11473P on 20.08.2015

Content

Зміст

Вісник ХНУ, серія «Фізика», вип. 29, 2018. с. 6-10

PACS: 81.40.Lm; 81.40.Ef; 62.20.F-
UDC: 539.382.2

Dislocation-kinetic approach to tensile stress-strain curve calculation for “flat” aluminum polycrystals

E.E. Badiyan, A.G. Tonkopryad, O.V. Shekhovtsov

V.N. Karazin Kharkiv National University, Svoboda Sq. 4, Kharkiv, 61022,
evgeny.e.badiyan@univer.kharkov.ua, shekhovtsov@yahoo.com.

The dislocation-kinetic approach is used for the stress-strain curve calculation for "flat" pure polycrystals of metals with average grain sizes d in the range from 10 to 500 μm and a thickness $D > 2d$ which were stressed in tension at a constant strain rate and moderate temperatures. The strain-hardening of "flat" pure aluminum polycrystals has been theoretically studied on the basis of the solution of the kinetic equation for the dislocation density. The effects of reduction in the conditional yield strength and strain-hardening coefficient and deviation from the Hall–Petch relation with decreasing specimen thickness have been found.

Keywords: "flat" pure polycrystals of metals; strain-hardening; tensile stress-strain curve; kinetic equation for the dislocation density.

Дислокаційно-кінетичний підхід застосовано для розрахунку деформаційної кривої "плоских" чистих полікристалів металів із середніми розмірами зерен d в інтервалі від 10 до 500 μm і товщиною $D > 2d$, які деформуються за умов одноосного розтягу з постійною швидкістю деформації при помірних температурах. На основі рішення кінетичного рівняння для густини дислокацій теоретично досліджено деформаційне зміцнення "плоских" чистих полікристалів алюмінію. Виявлено зниження умовної границі плинності, коефіцієнта деформаційного зміцнення і відхилення від співвідношення Холла-Петча при зменшенні товщини зразків.

Ключові слова: "плоскі" чисті полікристали металів; деформаційне зміцнення; крива розтягування; кінетичне рівняння для густини дислокацій.

Дислокационно-кинетический подход использован для расчета деформационной кривой "плоских" чистых поликристаллов металлов со средними размерами зерен d в интервале от 10 до 500 μm и толщиной $D > 2d$, деформированных в условиях одноосного растяжения с постоянной скоростью деформации при умеренных температурах. На основе решения кинетического уравнения для плотности дислокаций теоретически исследовано деформационное упрочнение "плоских" чистых поликристаллов алюминия. Обнаружено снижение условного предела текучести, коэффициента деформационного упрочнения и отклонение от соотношения Холла-Петча при уменьшении толщины образцов.

Ключевые слова: "плоские" чистые поликристаллы металлов; деформационное упрочнение; кривая растяжения; кинетическое уравнение для плотности дислокаций.

Introduction

The microscopic dislocation theory of a polycrystal's ductility is based on kinetic equations that describe the evolution of the dislocation density in a material with an increase of plastic deformation [1, 2]. The dislocation-kinetic approach makes it possible to obtain the dependence of the flow stress on the average grain size, temperature, degree and rate of deformation. The hardness and ductility characteristics of metal polycrystals can depend not only on the average grain size d, but also on the transverse size D (thickness or diameter) of tensile specimens. In [3], the interaction of the size factors D and d is analyzed using the kinetic equation for the dislocation density and the effects of the reduction in hardness and the deviation from the Hall-Petch relation during the plastic deformation of specimens with a micro- and nanograin structure with a decrease in their transverse size are theoretically considered. Investigation of the strain-hardening of "flat" * polycrystals with average grain sizes in the range from 10 to 500 μm is of interest. Both average grain size and specimen thickness should influence on the plastic flow of such sheets.

Equation for evolution of dislocation density in "flat" pure polycrystalline specimens

In pure polycrystalline materials, which were stressed in uniaxial tension at a constant strain rate $\dot{\varepsilon}$, given that the diffusion mechanisms for the dislocation annihilation in the boundaries and in the body of grains are absent at low and moderate temperatures, the change in average dislocation density ρ with increasing shear deformation $\gamma = m\varepsilon$, where $m = 3{,}05$ is the Taylor factor, can be written according to [2] as

$$\frac{d\rho}{d\gamma} = \frac{\beta}{bd} + k_f \rho^{1/2} - k_a \rho \,. \qquad (1)$$

In this expression, the first two terms on the right-hand side describe the accumulation of dislocations in a polycrystalline material due to the presence of grain boundaries (b is the Burgers vector, β describes the intensity of dislocation accumulation in grains because the grain size limits the mean free path length of dislocations) and the dislocation multiplication by double cross-slip of screw dislocations (k_f describes the intensity of dislocation multiplication on forest dislocations), and the third term describes the decrease in the dislocation density due to annihilation of the screw portions of dislocation loops (k_a is the coefficient of annihilation of screw dislocation). In general, the coefficient β which is defined as the relative fraction of grains contributing to the grain-boundary hardening can be found as $\beta = 1 - \Delta S / S$, where ΔS is the total area of grains in the specimen cross section which are directly adjacent to its surface, S is the cross-sectional area of the specimen. For specimens with a rectangular cross section, we can write

$$\beta = 1 - \left(\frac{2d}{D} + \frac{2d}{w} - \frac{4d^2}{wD} \right). \qquad (2a)$$

In specimens, which were investigated in this study, $2d < D << w$, so

$$\beta = 1 - \frac{2d}{D} \,. \qquad (2b)$$

We can see that the grain-boundary hardening depends on the ratio of d- and D-factors [3]. If only two grains are in the cross section of the specimen ($2d = D$), so that both are surface, the grain-hardening is practically absent and the coefficient β is zero.

Equation (1) is used for the theoretical description of strain-hardening of polycrystalline metals with average grain sizes in the range from 10 to 500 μm [2]. It is assumed that the transverse size D (thickness or diameter) of the deformed specimens is much higher than the average grain size d, so that the number $N = D/d$ of barriers in the form of grain boundaries in the specimen thickness is significantly greater than 1 and $\beta = 1$. In such samples, the flow stress is controlled by the grain size (d-factor) [3].

In [4, 5], the kinetic equation for the change in the dislocation density with increasing shear deformation in a single crystal is formulated:

$$\rho \frac{d\rho}{d\gamma} = \left(\frac{n_V}{b} + \left(\frac{S_S}{V} \right) \frac{n_S}{b} \right) + (k_m - k_{im} + k_f \rho^{1/2}) \rho - k_a \rho^2 . \qquad (3)$$

Here the terms in the first bracket on the right-hand side describe the work of dislocation sources inside a crystal with a bulk density n_V and surface dislocation sources with a density n_S. The terms in the second bracket describe the dislocation multiplication processes by double cross-slip on obstacles of non-deformation origin (the coefficient k_m), for example, the accumulation of impurity atoms, and deformation origin (on forest dislocations, the coefficient $k_f \approx 10^{-2} / b$), and also the immobilization of dislocations on obstacles (the coefficient k_{im}). The two coefficients depend on the D-factor in the kinetic equation (3) [6]. Thus, the departure of dislocations from a thin crystal through its surface (the annihilation of dislocations with the surface) leads to their loss from the multiplication process. Since the total path length of dislocations through the crystal is equal to the ratio D / m_e , where $m_e = \sin \varphi$, φ is the angle between the slip plane and the tensile axis, then $k_{im} = \sin \varphi / bD$. In addition, the contribution of surface dislocation sources to the process of generating dislocations at the initial stage of crystal deformation increases with increasing ratio S_S / V.

If the crystal is pure, then we can neglect the terms with n_V and k_m in (3) [6, 7]. Then equation (3) takes the form

$$\rho \frac{d\rho}{d\gamma} = \left(\frac{S_S}{V} \right) \frac{n_S}{b} - k_{im} \rho + k_f \rho^{3/2} - k_a \rho^2 . \qquad (4)$$

In large crystals, the first two terms on the right-hand side of (4) give an insignificant contribution to the evolution of the dislocation density [7]. However, their role increases with decreasing thickness of the specimen D. Dimensional effects arise that were investigated in [3, 6, 7]. For values of D less than some critical value, we can neglect the last two terms in (4), and we obtain a kinetic equation for the dislocation density in micro- and nanoscale crystals with allowance for only the D-factor [3, 7]:

$$\rho \frac{d\rho}{d\gamma} = \frac{n_S}{bL_F} - \frac{m_e}{bD} \rho \,, \qquad (5)$$

where L_F is the length of the Frank-Read source.

Simultaneous action of d- and D-factors in micro- and nanocrystalline pure samples, which had a transverse dimension in the micro- and nanoscale, was theoretically investigated in [3]. To this end, the terms from the right-hand sides of (1) and (5) were included in the kinetic equation. The term k_f was neglected because the average grain size was small. As a result, the following equation was obtained

* In this study, specimens with a rectangular cross section whose sizes are related by the inequality $D << w < l$, where D is the thickness of the specimen, w and l are its width and length respectively, and the ratio of the specimen surface area to its volume $S_S / V >> 1$ cm^{-1} are called "flat".

https://doi.org/

$$\rho\frac{d\rho}{d\gamma}=\frac{n_S}{b\delta_S D}+\frac{\beta(D,d)}{bd}\rho-\frac{m_e}{bD}\rho-k_a\rho^2. \quad (6)$$

Here it is taken into account that $L_F = \delta_S D$, where the parameter $\delta_S < 1$ determines the influence of various factors on the density and action intensity of dislocation sources.

In this paper, the combined action of *d*- and *D*-factors in "flat" pure polycrystalline specimens of metals with average grain sizes d in the range from 10 to 500 μm, which corresponds to conventional polycrystals [2], and a thickness $D > 2d$ is theoretically studied. To this end, all the terms from the right-hand sides of equations (1) and (4) were included in the kinetic equation for the dislocation density, as a result of which it acquired the form

$$\rho\frac{d\rho}{d\gamma}=\frac{\beta}{bd}\rho+\left(\frac{S_S}{V}\right)\frac{n_S}{b}+, \quad (7)$$
$$+k_f\rho^{3/2}-k_{im}\rho-k_a\rho^2$$

where

$$\frac{S_S}{V}=2\left(\frac{1}{D}+\frac{1}{w}\right)\approx\frac{2}{D}. \quad (8)$$

Tensile stress-strain curve calculation based on equation of dislocation kinetics

To obtain the tensile stress-strain curve $\sigma(\varepsilon, d, D)$, we transform equation (7) using expressions $\gamma = m\varepsilon$, $\sigma = m\tau$ and the Taylor equation $\tau = \alpha\mu b\rho^{1/2}$, in which α is the interaction constant of dislocations with one another, μ is the shear modulus, to the form

$$\frac{\sigma^3 d\sigma}{d\varepsilon} = -\frac{mk_a}{2}(\sigma^4+a_1\sigma^3+a_2\sigma^2+a_3), \quad (9a)$$

where

$$a_1=-m\alpha\mu b\frac{k_f}{k_a},$$

$$a_2=-\left(\frac{\beta}{bdk_a}-\frac{k_{im}}{k_a}\right)(m\alpha\mu b)^2, \quad (9b)$$

$$a_3=-\left(\frac{S_S}{V}\right)\frac{n_S}{bk_a}(m\alpha\mu b)^4.$$

After that, we integrate (9a) and obtain the dependence of the flow stress on deformation in an implicit form:

$$-\frac{2}{mk_a}(A_1\ln|\sigma-\sigma_1|+A_2\ln|\sigma-\sigma_2|+$$
$$+\frac{1}{2}A_3\ln|\sigma^2+\xi_1\sigma+\xi_2|+ \quad (10a)$$
$$+\frac{(-(1/2)\xi_1A_3+A_4)}{\sqrt{\xi_2-(\xi_1/2)^2}}\times$$
$$\times\operatorname{arctg}((\sigma+\xi_1/2)/\sqrt{\xi_2-(\xi_1/2)^2}))+C=\varepsilon.$$

The integration constant C is determined from condition

$$\sigma(0)=m\alpha\mu b\rho_0^{1/2}, \quad (10b)$$

where ρ_0 is the initial dislocation density at $\varepsilon = 0$. It is noted in [2] that the ρ_0 is due to the activation of dislocation sources in the grain boundaries: $\rho_0 = \beta_0/db$, where β_0 is the parameter that characterizes the effectiveness of grain boundaries as sources of dislocations and depends on the density of grain-boundary sources.

In (10a),

$$\sigma_{1,2}=-\frac{1}{2}\left(\frac{a_1}{2}-\left(\frac{a_1^2}{4}-a_2+y_1\right)^{1/2}\right)\pm$$
$$\pm\frac{1}{2}\sqrt{\left(\frac{a_1}{2}-\left(\frac{a_1^2}{4}-a_2+y_1\right)^{1/2}\right)^2-4\left(\frac{y_1}{2}-\left(\frac{y_1^2}{4}-a_3\right)^{1/2}\right)}, \quad (10c)$$

where

$$y_1=\left(-q/2+\left((p/3)^3+(q/2)^2\right)^{1/2}\right)^{1/3}+$$
$$+\left(-q/2-\left((p/3)^3+(q/2)^2\right)^{1/2}\right)^{1/3}+a_2/3, \quad (10d)$$

$$p=-a_2^2/3-4a_3,$$
$$q=2(-a_2/3)^3+8a_2a_3/3-a_1^2a_3. \quad (10e)$$

The quantities A_1, A_2, A_3, A_4 are defined as a solution of the system of equations

$$A_1+A_2+A_3=1$$
$$(\xi_1-\sigma_2)A_1+(\xi_1-\sigma_1)A_2+(-\sigma_1-\sigma_2)A_3+A_4=0$$
$$(\xi_2-\xi_1\sigma_2)A_1+(\xi_2-\xi_1\sigma_1)A_2+\sigma_1\sigma_2A_3+(-\sigma_1-\sigma_2)A_4=0 \quad (10f)$$
$$(-\xi_2\sigma_2)A_1+(-\xi_2\sigma_1)A_2+\sigma_1\sigma_2A_4=0$$

in which

$$\xi_1=a_1/2+\left((a_1/2)^2-a_2+y_1\right)^{1/2}, \quad (10g)$$
$$\xi_2=y_1/2+\left((y_1/2)^2-a_3\right)^{1/2}.$$

Figure 4 shows an example of the tensile stress-strain curve for polycrystalline aluminum calculated according to (10). In the calculations, the parameter values given in [2] were used (Table 1). For the density of surface dislocation sources, the estimated value $n_S = 10^6$ cm^{-2} was taken according to [6]. When calculating the immobilization coefficient k_{im}, we assumed that $m_e = \sin\pi/4 = 1/\sqrt{2}$.

Table 1.

Parameter values for polycrystalline Al used in calculations in accordance with formulas (10) given in [2].

μ, GPa	b, nm	α	k_a	β_0
27	0,286	0,32	11	10^{-3}

The dependence in Fig. 1 is ambiguous. It is seen from (10a) that the function $\sigma(\varepsilon)$ has an asymptote at a value of $\sigma = \sigma_1$ when $\ln|\sigma-\sigma_1| \to -\infty$ (this does not apply to $\ln|\sigma-\sigma_2|$, since σ_2 takes negative values as indicated by the calculation).

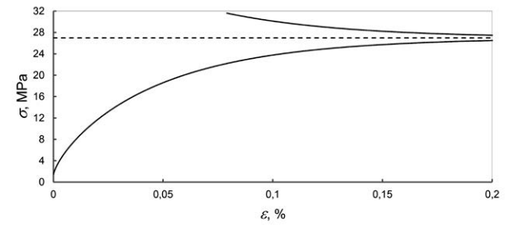

Fig. 1. Dependence of the flow stress on the degree of plastic deformation with the asymptote $\sigma_1 = 27$ MPa for a "flat" pure polycrystalline Al specimen with D = 500 μm, w = 2 cm, d = 100 μm.

The upper segment of the dependence $\sigma(\varepsilon)$ which is partially shown in Fig. 1 has negative values of the strain-hardening coefficient $\theta = d\sigma/d\varepsilon$. The presence of segments with positive and negative values θ is associated according to [6] with the competition of processes of generation of dislocations and their departure. The equilibrium between these processes is established with increasing deformation (the asymptote $\sigma = \sigma_1$ in Fig. 1). A possible physical interpretation of the ambiguous nature of the dependences $\sigma(\varepsilon)$ is discussed in [6]. For example, it consists in the fact that the deforming stress will change stepwise between the upper and lower segments of the dependence $\sigma(\varepsilon)$ under conditions of strong slip heterogeneity. It was observed in experiments on the compression of gold microcrystals [8, 9]. In the absence of a noticeable slip heterogeneity (high density of dislocation sources), dependences $\sigma(\varepsilon)$ become single-valued and smooth in the type of the lower segment in Fig. 1.

Yield strength and strain-hardening of "flat" polycrystal

According to the empirical Hall-Petch relation [10, 11]

$$\sigma_y=\sigma_0+K_y d^{-1/2}, \quad (11)$$

where σ_y is the conditional yield strength, K_y is the Hall-Petch coefficient, the parameter σ_0 corresponds to the yield strength of a single crystal. In calculations based on formulas (10) in the interval of average grain sizes of "flat" Al polycrystals from 10 to 70 μm for thicknesses of 500, 250 and 150 μm, the deviation from the linear dependence $\sigma_{0,2} - d^{-1/2}$ (11) is manifested at D = 250 μm and it becomes good is noticeable at D = 150 μm (Fig. 2). Fig. 3 shows that the conditional yield strength increases with increasing thickness in specimens with different average grain sizes.

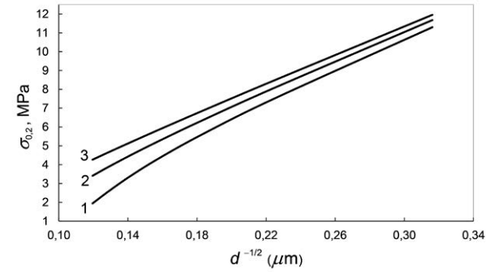

Fig. 2. Dependence of the conditional yield strength on the average grain size for "flat" pure polycrystals Al of width w = 2 cm with different thicknesses: 1 - D = 150 μm, 2 - D = 250 μm, 3 - D = 500 μm.

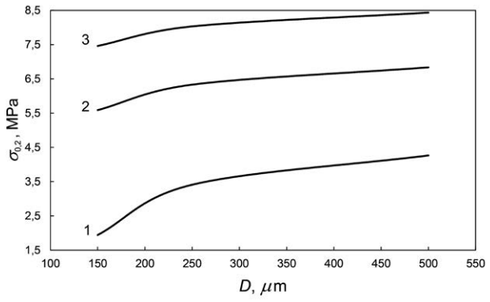

Fig. 3. Dependence of the conditional yield strength on the specimen thickness for "flat" pure polycrystals Al of width w = 2 cm with different average grain sizes: 1 - d = 70 μm, 2 - d = 30 μm, 3 - d = 20 μm.

The combined action of *d*- and *D*-factors causes the appearance of yet another dimensional effect which manifests itself in the dependence of the strain-hardening coefficient of a "flat" polycrystal on its thickness. Taking (9a) into account, we obtain for the strain-hardening coefficient:

$$\theta=\frac{d\sigma}{d\varepsilon} = -\frac{mk_a}{2}(\sigma+a_1+a_2\sigma^{-1}+a_3\sigma^{-3}). \quad (12)$$

Here the flow stress σ is given by (10). The results of calculations using formula (12) are shown in Fig. 4. The Dependences $\sigma_{0,2}(D)$ и $\theta(D)$ in Fig. 3 and 4 are amplified as $2d$ approaches to D (the coefficient β tends to zero in accordance with (2b)).

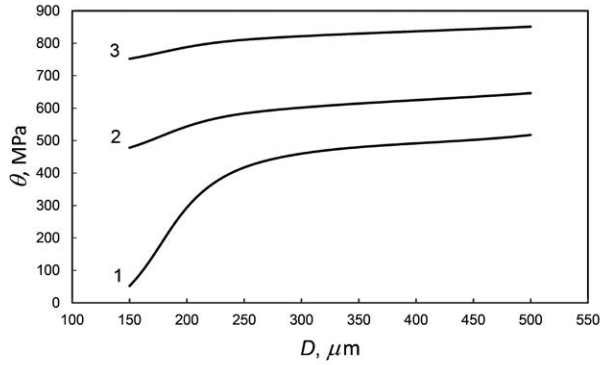

Fig. 4. Dependence of the strain-hardening coefficient on the specimen thickness for "flat" pure polycrystals Al of width $w = 2$ cm with different average grain sizes (1 - $d = 70$ μm, 2 - $d = 30$ μm, 3 - $d = 20$ μm) at $\varepsilon = 1\%$.

The determination of the strain-hardening coefficient at a deformation ε = 1% for the values of the average grain size in the range from 100 to 250 μm as a function of the specimen thickness 600 μm < D < 1200 μm leads qualitatively to the same results as in Fig. 4. At the thickness D = 1200 μm, the conditions $D << w$ and $S_S / V >> 1$ cm^{-1} which were formulated for "flat" polycrystals are almost at the limit. For specimens with the average grain size d = 500 μm, the condition $D > 2d$ is satisfied for $D > 1000$ μm. Thus, the values of $d \approx 500$ μm and $D \approx 1200$ μm are near the applicability limits of the model of strain-hardening of "flat" polycrystals.

Conclusions

1. On the basis of the dislocation-kinetic equation, a relation for calculating the stress-strain curve $\sigma(\varepsilon, d, D)$ for "flat" pure polycrystals of metals with average grain sizes in the range from 10 to 500 μm, such that $2d < D$, which were stressed in uniaxial tension at a constant strain rate and moderate temperatures was obtained.
2. Using the example of the analysis of the calculated dependence $\sigma(\varepsilon, d, D)$ for "flat" pure Al polycrystals with a width $w = 2$ cm and different thicknesses in the range $150 < D < 1200$ μm, it was established that the interaction of d- and D-factors causes a reduction in the conditional yield strength and deviation from the Hall-Petch relation with a decrease in the specimen thickness. The dimensional effect is also manifested in a reduction in the strain-hardening coefficient of a "flat" pure Al polycrystal with decreasing its thickness.
3. The kinetic equation (7) and the solution (10) describe the strain-hardening of a "flat" polycrystal as a result of an increase in the average dislocation density in it without taking into account their inhomogeneous distribution in the material. When studying strain-hardening and the formation of dislocation structures for large plastic deformations, it is necessary to include collective effects in ensembles of strongly interacting dislocations that lead to the formation of cellular and fragmented dislocation structures.

References

1. Kocks U.F., Mecking H. Prog Mater Sci. 48, 171 (2003).
2. Malygin G.A. Fizika Tverd. Tela, 49, V. 6, 961 (2007).
3. Malygin G.A. Fizika Tverd. Tela, 54, V. 3, 523 (2012).
4. Malygin G.A. Fizika Tverd. Tela, 35, V. 5, 1328 (1993).
5. Malygin G.A. Fizika Tverd. Tela, 35, V. 6, 1698 (1993).
6. Malygin G.A. Fizika Tverd. Tela, 52, V.1, 48 (2010).
7. Malygin G.A. Uspekhi Fiz. Nauk, 181, V. 11, 1129 (2011).
8. Greer J.R., Oliver W.C., Nix W.D. Acta Mater., 53, 1821 (2005).
9. Greer J.R., Nix W.D. Phys. Rev. B, 73, 245410 (2006).
10. Hall E.O. Proc. Phys. Soc., 64B, 747 (1951).
11. Petch N.J. Journ. Iron Steel Inst., 173, 25 (1953).

Вісник ХНУ, серія «Фізика», вип. 29, 2018. с. 11-15

PACS 05.45.Xt, 74.50.+r, 85.25.Cp
УДК: 537.312.62

Electrical properties of stacks of many long Josephson junctions

A. Grib[1], R. Vovk[1], S. Savich[1], V. Shaternik[2]

[1]*Department of Physics, V. N. Karazin Kharkiv National University, 4 Svobody Sq., Kharkiv 61022, Ukraine*
[2]*G.V. Kurdyumov Institute for Metal Physics, N.A.S. of Ukraine, 36 Academician Vernadsky Boulevard, UA-03142 Kyiv, Ukraine*

We investigated numerically IV-characteristics and power of emission from stacks with various quantities of long Josephson junctions (up to 6 junctions) which interacted inductively with each other. Parameters of junctions were chosen close to those for MoRe-Si(W)-MoRe heterostructures. We set Gaussian spread of about 0.01% of critical currents along junctions. Electrical properties of a stack consisted of three junctions was investigated in details. Zero-field steps at voltages corresponding to frequencies of various modes of electromagnetic waves in the stack were found in the IV-characteristic. We showed that positions of zero-field steps in IV-curves were in good agreement with predictions of the theory. The highest maximum of power of emission corresponded to the so-called in-phase mode at which all voltages over junctions in the stack oscillate in-phase. Considering stacks with many junctions, we showed that power of emission at the voltage of the resonance which corresponds to the in-phase mode is proportional to the square of quantity of long junctions in the stack that is the characteristic of coherent emission.

Keywords: Josephson junctions; coherent emission; synchronization; zero-field steps.

Ми дослідили чисельно вольт - амперні характеристики та потужність випромінювання пачок з різною кількістю контактів Джозефсона (до 6 контактів), що взаємодіють індуктивно один з одним. Параметри контактів були вибрані близькими до параметрів гетероструктур MoRe-Si(W)-MoRe. Ми задали гаусів розбіг критичних струмів близько 0.001% вздовж контактів. Електричні властивості пачки, яка складалася з трьох контактів, були детально досліджені. Сходинки нульового поля при напругах, які відповідали частотам різних мод електромагнітних хвиль в пачці були знайдені на вольт - амперній характеристиці. Ми показали, що положення сходинок нульового поля на вольт - амперних характеристиках добре узгоджені з теоретичними передбаченнями. Найбільший максимум емісії відповідав так званій синфазній моді, при якій всі напруги на контактах осцилюють синфазно. Розглянувши пачки з багатьма контактами, ми показали, що потужність емісії при резонансній напрузі, яка відповідає синфазній моді, пропорційна квадрату числа довгих контактів у пачці, що є характерним для когерентної емісії.

Ключові слова: контакти Джозефсона; когерентна емісія; синхронізація; сходинки нульового поля.

Мы исследовали численными методами вольт - амперные характеристики и мощность эмиссии от пачек с различным количеством длинных джозефсоновских переходов (до 6 переходов), которые индуктивно взаимодействовали друг с другом. Мы задали гауссов разброс 0.01% критических токов вдоль переходов. Электрические свойства пачки, состоящей из трёх переходов, были подробно исследованы. Ступеньки нулевого поля при напряжениях, соответствующих частотам различных мод электромагнитных волн в пачке, были найдены на вольт - амперной характеристике. Мы показали, что позиции ступенек нулевого поля на вольт - амперных кривых находятся в хорошем согласии с предсказаниями теории. Наивысший максимум мощности эмиссии соответствовал так называемой синфазной моде, в которой все напряжения на контактах в пачке осциллируют синфазно. Рассматривая пачки со многими контактами, мы показали, что мощность эмиссии при резонансном напряжении, которое соответствует синфазной моде, пропорциональна квадрату количества длинных переходов в пачке, что является характерным для когерентной эмиссии.

Ключевые слова: джозефсоновские переходы; когерентная эмиссия; синхронизация; ступеньки нулевого поля.

Introduction

Recently, the huge progress was made in the creation of sources of coherent emission made of many intrinsic Josephson junctions on the base of high-temperature superconductors [1-3]. These sources work in the sub-terahertz and terahertz region of frequencies [1]. This gives the possibility to develop ultrafast nonlinear terahertz spectrometers, terahertz imaging systems, the high-resolution Michelson interferometer [1-3]. It is proved experimentally and theoretically that the mechanism which leads to strong synchronization of radiation of junctions in the stack is connected with the interaction of Josephson generation with cavity resonances and the formation of self-resonant steps in the IV-characteristic in the absence of externally applied magnetic field (the so-called zero-field steps) [4, 5]. In the present paper we apply basic ideas of the developed theory to stacks of junctions made on the base of low-temperature superconductors which can be more stable sources.

https://doi.org/

At first we discuss the formation of zero-field steps in the solitary Josephson junction. Zero-field steps are close related to Fiske steps which appear at voltages which correspond to frequencies of geometrical resonances in the system when the Josephson junction is placed in some magnetic field [6, 7]. However, when the magnetic field is absent, steps in the IV-curve can not appear in the homogeneous junction [8]. If the distribution of critical currents is inhomogeneous and symmetrical (just this case we discuss in the paper), zero-field steps appear at voltages V_p that correspond to even geometrical resonances:

$$V_p = \frac{\Phi_0 c p}{D}, \qquad (1)$$

where Φ_0 is the quantum of magnetic flux, c is the velocity of light in the junction, D is the size of the junction and p=1,2… is integer. It is proven also that some disorder of the distribution of critical currents leads to the formation of zero-field steps [9-11].

The theory of electric properties of stacks of Josephson junctions was developed and proved experimentally in Refs. [12-15]. One of the main results of this theory is that in the stack of m junctions with inductive interaction between superconducting layers the Fiske step is split to m branches. For example, the even Fiske step at the voltage V_p calculated from Eq. (1) is split to m branches which positions are determined as follows:

$$V_{p,p'}^{(m)} = \frac{\Phi_0 c p}{D}\sqrt{\frac{1}{1+2S\cos\left(\pi p'/(m+1)\right)}}, \qquad (2)$$

where $p' = 1...m$ is integer and S is the normalized constant of inductive coupling of layers [13]. However, it has been shown that in the stack of two junctions with disorder of critical currents zero-field steps are split also [9-11], and positions of steps in the IV-curve can be calculated from Eq. (2). The coefficient $\alpha = L_f / L$ which characterizes the relation of the mutual inductance L_f between junctions to the inductance L of the junction in a stack [9-11] coincides with the constant of inductive coupling S in Eq. (2). Due to the interaction between layers, some modes of excitations are formed in the stack and each of the branches of the zero-field step corresponds to its own mode. Amongst these modes there is the mode of fully coherent oscillations of all junctions (it is the so-called in-phase or coherent mode with $p' = m$ which corresponds to the branch with highest voltage). Just at the branch of the coherent mode oscillations of voltages over junctions can be fully synchronized.

In the present paper we investigate numerically IV-characteristics and power of coherent emission from stacks of long Josephson junctions. Parameters of junctions and the whole stack are chosen close to those for MoRe-Si(W)-MoRe heterostructures which have appropriate values of the characteristic voltage and the density of critical current [16-18]. We discuss the IV-curve of the three-junction stack in details and prove the existence of the coherent mode. Then we investigate stacks with different numbers of long junctions and investigate the dependence of emitter power on the quantity of junctions at voltages of the in-phase mode.

The model

For calculations of IV-characteristics and power of emission from the stack of many long junctions we follow the method developed in Ref. [9]. Each of the long junctions with indices i=1…m is divided to n segments with indices j=1…n. Each of the segments has the capacitance $C_{i,j}$ (we suppose $C_{i,j}$=C for all segments) and the resistance $R_{i,j}$. Loops between centers of segments in each of the long junctions has the inductance L. Current conservation conditions and conditions of quantization of magnetic flux are as follows:

$$\frac{\Phi_0 C}{2\pi}\frac{d^2\varphi_{i,j}}{dt^2} + \frac{\Phi_0}{2\pi R_{i,j}}\frac{d\varphi_{i,j}}{dt} + I_{ci,j}\sin\varphi_{i,j} = = I_b - I^R_{i,j-1,j} + I^R_{i\,j,j+1}, \qquad (3)$$
$$i = 1...m, \; j = 2...n-1,$$

$$-L_f I^R_{i-1,j-1,j} + L I^R_{i,j-1,j} - L_f I^R_{i+1,j-1,j} + \frac{\Phi_0}{2\pi}\left(\varphi_{i,j-1} - \varphi_{i,j}\right) = 0, \qquad (4)$$
$$i = 2...m-1, \;\; j = 2...n,$$

where I_b is the bias current (we suppose that the same bias current flows through all segments, so the total bias current through the stack is equal to I=nI_b), $\varphi_{i,j}$ is the difference of the phase of the order parameter across the segment, $I_{Ci,j}$ is the critical current of the segment, Φ_0 is the quantum of magnetic flux, $I^R_{i,j-1,j}$ is the ac current in the loop between two segments with indices j-1 and j which are placed within the i-th long junction, L_f is the mutual inductance between adjacent long junctions. To describe emission from the system, we attached contours with the resistance R_e, the inductance L_e and the capacitance C_e to the upper and lower superconducting electrodes at both ends of the stack. Then for junctions with indices j=1 and j=n such equations are valid (boundary conditions):

$$\frac{\Phi_0 C}{2\pi}\frac{d^2\varphi_{i,1}}{dt^2} + \frac{\Phi_0}{2\pi R_{i,1}}\frac{d\varphi_{i,1}}{dt} + I_{ci,1}\sin\varphi_{i,1} = = I_b + I^R_{i,1,2} - \frac{dq}{dt}, \qquad (5)$$
$$i = 1...m,$$

$$\frac{\Phi_0 C}{2\pi}\frac{d^2\varphi_{i,n}}{dt^2} + \frac{\Phi_0}{2\pi R_{i,n}}\frac{d\varphi_{i,n}}{dt} + I_{ci,n}\sin\varphi_{i,n} = = I_b - I^R_{i,n-1,n} + \frac{dq}{dt}, \qquad (6)$$
$$i = 1...m,$$

$$L_e\frac{d^2q}{dt^2} + R_e\frac{dq}{dt} + \frac{q}{C_e} = \frac{\Phi_0}{2\pi}\sum_{i=1}^{m}\frac{d\varphi_{i,j}}{dt}, \qquad (7)$$
$$j = 1, n,$$

where q is the charge that passes the inductance L_e. Normalized to the quantity of long junctions voltage over the stack is equal to

$$V = \frac{\Phi_0}{2\pi}\frac{1}{mn}\left\langle\sum_{j=1}^{n}\left(\sum_{i=1}^{m}\frac{d\varphi_{i,j}}{dt}\right)\right\rangle, \qquad (8)$$

where the sign $\langle ... \rangle$ means the averaging on time which is much large than the period of Josephson generation.

Ac power of emission P_j from ends of the system was calculated as follows:

$$P_j \approx \frac{1}{R_a}\left\langle\left[\frac{\Phi_0}{2\pi}\sum_{i=1}^{m}\left(\frac{d\varphi_{i,j}}{dt} - \left\langle\frac{d\varphi_{i,j}}{dt}\right\rangle\right)\right]^2\right\rangle, \qquad (9)$$
$$j = 1, n.$$

The system of Eqs. (3)-(7) was solved by the method of Runge-Kutta. IV-characteristics and power of emission fro the left end of the stack P_1 were calculated with the use of Eqs. (8), (9).

Results and Discussion

Now we discuss main conditions for the formation of zero-field steps. One of them is the mentioned in the Section 1 inhomogeneous distribution of critical currents along the junction. In junctions made on the base of low-temperature superconductors it is impossible to create the inhomogeneous distribution due to self-heating like it is in high-temperature superconductors [11]. The necessary distribution can be created by some disorder of critical currents. Another condition for the appearance of zero-field steps is that the frequency of the geometrical resonance should be inside the interval of frequencies of Josephson generation. To fulfill this condition, the stack should have a length of order of hundred micrometers. This means that junctions in such a stack have large capacitances. However, zero-field steps in IV-curves of junctions with large capacitances are hard to reveal. Both mentioned conditions are satisfied in heterostructures which consist of superconducting electrodes made of molybdenum-rhenium alloy with the critical temperature of about 9 K and a hybrid tunnel barrier made of silicon with nanoclusters of (the MoRe-Si(W)-MoRe heterostructure) [16-18]. These junctions have some capacitance due to non-fully grown nanoclusters. Our first treatment of IV-curves of such structures showed that zero-field steps appear in such structures [19].

At first, we calculated IV-characteristics and power of emission for the stack of three Josephson junctions with values of parameters close to those for MoRe-Si(W)-MoRe heterostructures. For the correct choice of parameters we introduced the fictive width of the stack $W = 2.5\cdot10^{-4}$ m. The length of the stack was $D = 1.3\cdot10^{-4}$ m. The density of critical current was $J_c = 9\cdot10^5$ A/m^2, the critical voltage was $V_c = 2$ mV, the thickness of the superconducting layer was $\tau = 60\cdot10^{-9}$ m, the thickness of the barrier was $\delta = 2\cdot10^{-9}$ m, the velocity of light in the junction was $c = 4.9\cdot10^7$ m/s, the capacitance per square area was $C_d = 3.5\cdot10^{-3}$ F/m^2. Then we divided each junction in the stack to 60 segments with the length $\xi = D/n = 2.17\cdot10^{-6}$ m and found for one segment $C = 1.9\cdot10^{-12}$ F and the McCumber parameter $\beta_C = 47.8$. The Josephson length of penetration of magnetic field was $\lambda_J = 5.6\cdot10^{-5}$ m, so the relation $\xi/\lambda_J << 1$ was fulfilled. The value of the inductance of the segment L was defined from the relation $L = \xi^2/(c^2C) = 1.01\cdot10^{-15}$ H. The value of the parameter S=0.21 was calculated with the use of Ref. [13]. We set Gaussian spread of critical currents $10^{-4}\cdot I_c$ (or 0.01%) for each of the segments. Parameters of external contours were L_e=10^{-6} H, R_e=300 Ohm, $C_e = 9.6\cdot10^{-14}$ F.

The calculated IV-characteristic of the three-junction stack is shown in Fig. 1a. In this plot we used reduced units, namely, $i = I_b/I_{ca}$ with I_{ca} is the averaged critical current, $v = V/Vc$, $p_j = P_j/(I_{ca}V_c)$. This IV-curve was obtained by means of sweeping of the bias current, i. e. the bias current in the hysteretic region was decreased to zero at the first sweep, then increased again above the hysteretic region, then was decreased to i=0.34 and then was increased again. According to Eq. (1), the zero-field step in the IV-characteristic of the solitary junction should be at $v_{p=1}$=0.39. For the stack with three junctions this zero-field step should split into three steps: $v_{p=1,\,p'=1}$=0.34, $v_{p=1,\,p'=2}$=0.39 and $v_{p=1,\,p'=3}$=0.47. These modes are called as the anti-phase mode, the decoupled mode and the in-phase mode, correspondingly [20]. Calculated positions of steps are shown in Fig. 1a by arrows. It is seen that arrows almost coincide with steps. The plot of emitted power on the voltage is shown in Fig. 1b. As it was expected, the highest maximum of $p1(v)$ is at the voltage $v_{p=1,\,p'=3}$=0.47, which corresponds to the frequency of the in-phase mode. Thus, we investigated electrical properties of the stack with three junctions with the small Gaussian distribution of critical currents and without applied magnetic field and found the good agreement of our numerical results for positions of zero-field steps and emitted radiation with predictions of the theory [12-15]. Note that earlier this theory was applied for Fiske steps of stacked junctions in magnetic field [13].

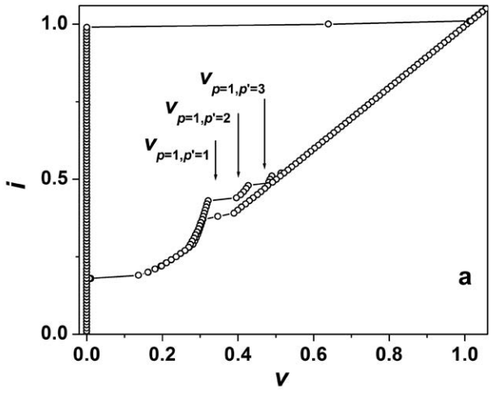

a

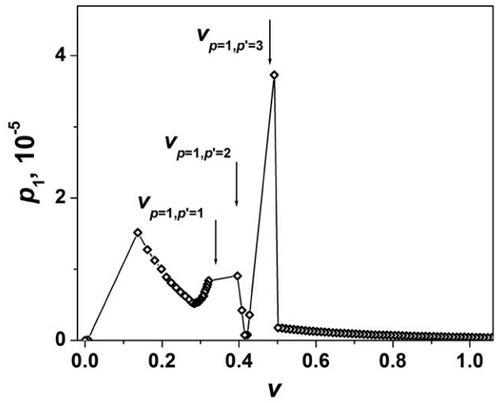

b

Fig. 1. 1(a): the IV-characteristic of the stack of three Josephson junctions. The curve is obtained during sweeping of the bias current. Positions of voltages of zero-field steps calculated with the use of Eq. (2) are marked by arrows. 1(b): the dependence of ac power on voltage.

Now we investigate the dependence of power of emission in many-junction stacks on the quantity of junctions in the stack. We used such values of parameters: W = 3.0•10-4 m, D = 1.0•10-4 m, Jc = 1•105 A/m2, $V_c = 4.73$ mV, $\tau = 50 \bullet 10^{-9}$ m, $\delta = 2 \bullet 10^{-9}$ m, $c = 6.7 \bullet 10^{7}$ m/s, $C_d = 3.5 \bullet 10^{-3}$ F/m^2, $n = 60$, $\xi = 1.67 \bullet 10^{-6}$ m, $C = 4.5 \bullet 10^{-14}$ F, $\beta_C = 62.0$, $\lambda_J = 3.7 \bullet 10^{-5}$ m, $L = 1.36 \bullet 10^{-14}$ H, $S = 0.21$, the Gaussian spread of critical currents was $10^{-5} \bullet I_c$ and parameters of external contours were $L_e = 10^{-6}$ H, $R_e = 300$ Ohm, $C_e = 2.3 \bullet 10^{-5}$ F. The first resonance step for the solitary junction calculated from Eq. (1) was equal to $V_{p=1} = 0.29 \bullet V_c$.

In calculations we decrease the bias current in the hysteretic region and define power of emission from maxima of the plot $P_1 = f(V)$ at voltages which correspond to in-phase modes. This method is usually used in experiments when the dc current-biased scheme is applied.

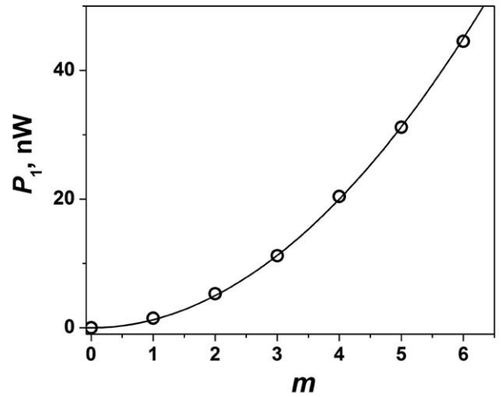

Fig. 2. The dependence of maximal power P_{1max} emitted from the stack on the quantity of junctions m in the stack. Solid line is the approximation of calculated data by the dependence $P_1(m) = Am^2$ with $A = 1.25 \bullet 10\text{-}9$ W.

The deficiency of this procedure is clearly seen from Fig. 1a. During the decrease of the bias current there is a jump of voltage from the resistive branch of the IV-curve to the step in the region of its bottom. The maximum of emission power is in the vicinity of the jump. The larger is the McCumber parameter the smaller is the jump, so it is hard to detect the solitary in-phase mode. Because the position of the right edge of the jump is defined by the step on the IV-curve, the obtained value of the power of emission at this point is the arbitrary point at the maximum. Therefore, we applied averaging of these values over 5-6 calculations of IV-curves with different steps.

The plot $P_1 = f(m)$ is shown in Fig. 2 (circles). The solid line in this plot is the dependence $P_1(m) = Am^2$ with the coefficient $A = 1.25 \bullet 10^{-9}$ W that is close to the value of emitted power for the solitary junction ($P_1(1) = 1.5 \bullet 10^{-9}$ W). It is seen that the approximation describes our data with good accuracy. According to the theory of synchronization [21], in the case of fully coherent emission the ac emitted power is proportional to the square of the quantity of junctions: $P_1(m) = P_1(1) \bullet m^2$, where $P_1(1)$ is power of emission of one solitary long junction, and in the case of fully decoupled junctions the power of emission is equal to $P_1(m) = P_1(1) \bullet m$. Thus, we make a conclusion that at the in-phase mode voltage oscillations across long Josephson junctions in stacks are synchronized. With the use of this mode one can create sources of coherent emission.

Conclusions

In this paper we investigated IV-characteristics and emission of stacks with different amount of Josephson junctions which interact inductively with each other. We set small Gaussian spread of critical currents (about $10^{-4} \bullet I_c$ or 0.01%) along junctions in stacks and found zero-field steps in IV-characteristics. We showed that voltages at which zero-field steps appeared can be calculated with the use of Eq. (2) of the theory [12-15] which was earlier applied to stacks placed in external magnetic field. This result is in agreement with our previous investigations [9-11] in which we found that the zero-field steps in a stack of two inductively interacting long Josephson junctions was split to two steps and positions of these steps in the IV-curve was defined by frequencies of normal modes. We also investigated the dependence of emitted power at the voltage which corresponds to the frequency of the in-phase mode and proved that voltages across long junctions in the stack oscillate in-phase.

Acknowledgement

This publication is based on the research provided by the grant support of the State Fund for Fundamental Research (project Ф76/36725).

References

1. Kurama Nakade et al., Scientific Reports, 6, 23178 (2016).
2. H. Minami et al., Phys. Rev. B, 89, 054503 (2014).
3. T. M. Benseman et al., Appl. Phys. Lett., 103, 022602 (2013).
4. L. Ozyuzer, et al., Science, 318, 1291 (2007).
5. A. E. Koshelev, L. N. Bulaevskii. Phys. Rev. B77, 014530 (2008).
6. I. O. Kulik. Zh. Eksp. Teor. Fiz. Pis. Red., 2, 134 (1965) [JETP Lett., 2, 84 (1965)].
7. Antonio Barone, Gianfranco Paternò. Physics and applications of the Josephson effect, John Wiley and sons, New York. (1982), 529 p.
8. C. Camerlingo, M. Russo, R. Vaglio, J. Appl. Phys., 53, 7609 (1982).
9. Alexander Grib and Paul Seidel, IEEE Trans. Appl. Supercond., 26, 1801004 (2016).
10. Alexander Grib and Paul Seidel, IEEE Trans. Appl. Supercond., 27, 1800604 (2017).
11. Alexander Grib, Paul Seidel and Masayoshi Tonouchi, Supercond. Sci. Technol., 30, 014004 (2017).
12. S. Sakai and P. Bodin, N. F. Pedersen, J. Appl. Phys., 73, 2411 (1993).
13. S. Sakai, A. V. Ustinov and H. Kohlstedt, A. Petraglia and N. F. Pedersen, Phys. Rev. B, 50, 12905 (1994).
14. R. Kleiner, P. Müller, H. Kohlstedt. N. F. Pedersen, S. Sakai, Phys. Rev.B, 50, 3942 (1994).
15. R. Kleiner, Phys. Rev.B, 50, 6919 (1994).
16. V. Shaternik, A. Shapovalov, O. Suvorov, N. Skoryk, and M. Belogolovskii, Low Temp. Phys., 42, 426 (2016).
17. V. E. Shaternik, A. P. Shapovalov, O. Yu. Suvorov, Low Temp. Phys. (Fiz. Nizk. Temp.), 43, 877 (2017).
18. V. E. Shaternik, A. P. Shapovalov, T. A. Prikhna, O. Y. Suvorov, M. A. Skorik, V. I. Bondarchuk, and V. E. Moshchil, IEEE Trans. Appl. Supercond., 27, 1800507 (2017).
19. A. Grib, S. Savich, R. Vovk, V. Shaternik, A. Shapovalov, P. Seidel, IEEE Trans. Appl. Supercond., in press.
20. C. Gorria, P. L. Christiansen, Yu. B. Gaididei, V. Muto, N. F. Pedersen, M. P. Soerensen, Phys. Rev. B, 66, 172503 (2002).
21. K. K. Likharev. Dynamics of Josephson junctions and circuits, Gordon and Breach, Philadelphia. (1991), 750 p.

Вісник ХНУ, серія «Фізика», вип. 29, 2018. с. 16-21

PACS: 67.25.dk; 67.25.dg ; 67.25.dm
УДК: 532.5.031; 532.5.032; 532.517.2; 532.517.3; 532.517.4;

An alternative explanation for the nonlinear behavior of the oscillating tuning fork immersed in He II

I. Gritsenko, T. Dubchak, K. Mykhailenko, G. Sheshin, S. Sokolov

B. Verkin Institute for Low Temperature Physics and Engineering of the National Academy of Sciences of Ukraine
Prospekt Nauky 47, Kharkov 61103, Ukraine
sheshin@ilt.kharkov.ua

Experiments have been carried out on the excitation of hydrodynamic flows in superfluid helium under forced vibrations of a quartz tuning fork immersed in a liquid. Nonlinear oscillations that arise with an increase in the driving force are investigated and are manifested by distortion of the shape of the resonant amplitude-frequency characteristic in comparison with Lorentz curves typical for an extremely small force. Nonlinear resonance curves are described using the Duffing equation, the parameters of which are established by comparing the theoretical calculation with the experimental data. Dependence of the velocity of vibrations of the tuning fork legs on the driving force established with the use of the Duffing equation, is close to that previously obtained for the quasi-laminar flow of He II and containing a cubic velocity contribution due to the mutual friction caused by scattering of phonons by quantized vortices in a turbulent flow.

Keywords: quartz tuning fork; turbulence in liquid helium; scattering of phonons by quantized vortices.

Проведено експерименти по порушенню гідродинамічних потоків у надплинному гелії при змушених коливаннях кварцового камертона, зануреного в рідину. Досліджено нелінійні коливання, які виникають при збільшенні сили, що змушує, і проявляються перекручуванням форми резонансної амплітудно-частотної характеристики в порівнянні з лоренцевими кривими, типовими для гранично малої сили. Нелінійні резонансні криві описані з використанням рівняння Дуффінга, параметри якого встановлені при порівнянні теоретичного розрахунку з експериментальними даними. Залежність швидкості коливань ніжок камертона від сили, що змушує, установлена з використанням рівняння Дуффінга, виявляється близької до залежності, раніше отриманої для квазіламінарного плину He II і утримуючої кубічний по швидкості внесок у силу взаємного тертя, обумовленої розсіюванням фононів на квантованих вихрах у турбулентному потоці.

Ключові слова: кварцовий камертон; турбулентність в рідкоу гелії; розсіювання фононів на квантованих вихорах.

Проведены эксперименты по возбуждению гидродинамических потоков в сверхтекучем гелии при вынужденных колебаниях кварцевого камертона, погруженного в жидкость. Исследованы нелинейные колебания, которые возникают при увеличении вынуждающей силы и проявляются искажением формы резонансной амплитудо-частотной характеристики по сравнению с лоренцевыми кривыми, типичными для предельно малой силы. Нелинейные резонансные кривые описаны с использованием уравнения Дуффинга, параметры которого установлены при сравнении теоретического расчета с экспериментальными данными. Зависимость скорости колебаний ножек камертона от вынуждающей силы. установленная с использованием уравнения Дуффинга, оказывается близкой к зависимости, ранее полученной для квазиламинарного течения He II и содержащей кубический по скорости вклад в силу взаимного трения, обусловленной рассеянием фононов на квантованных вихрях в турбулентном потоке.

Ключевые слова: кварцевый камертон; турбулентность в жидком гелии; рассеяние фононов на квантованных вихрях.

Introduction and task statement

One of the mostly used methods of studying the laminar and turbulent flow regimes in superfluid helium is the method of a quartz tuning fork immersed in a liquid. The quartz tuning fork differs favorably from the bodies of other geometry, first of all with high quality factor which attains ~ 10^6. Also essential is the availability of quartz tuning fork (they are manufactured in industry), as well as their high durability [1].

When working with tuning forks with the prongs of different sizes, one can change the frequency of the resonances and the form of the amplitude-frequency characteristic (AFC) [2]. Moreover, as established during an experimental study of the appearance and development of superfluid turbulence in the temperature range down to ~ *20 mK*, under increasing the velocity of movement of the tuning prongs up to *0.02 m/s* the shape of the resonant AFC starts to deform. This deformation

https://doi.org/

is explained in [2,3] as a result of the nonlinearity of tuning fork oscillations. Turbulent flows in He II at higher temperatures, *140* and *150 mK*, were investigated in Ref. 3 by the quartz tuning fork method. It was shown that the deviation from the linear dependence of the tuning fork velocity on the exciting force was observed at oscillation velocities exceeding *0.04 m/s*. The physical reason for the nonlinearity observed in [2,4] is, probably, the effect of an attached mass associated with quantum superfluid fluid vortices located in a thin layer of a liquid near the surface of a tuning fork, and there are the arguments [3] in favor of the fact that nonlinear deformations of AFC are connected with the appearance of an additional, nonlinear force of mutual friction due to the scattering of thermal excitations on the quantized vortices.

The observation of nonlinear effects at the excitation of the motion of He II by a quartz tuning fork calls an attention to the adequate description of the fork nonlinear resonance. The possibility of such a description appears when one uses the equation of a nonlinear oscillator [4,5] in the presence of an excitatory force. A separate case of the equation proposed in [4] is the Duffing equation [5], in which, unlike [4], the coefficient is set to zero with a quadratic displacement of the x term in the left-hand side and only the cubic term is available:

$$\frac{d^2x(t)}{dt^2} + \gamma\frac{dx(t)}{dt} + \omega_0^2 x(t) + \mu x^3 = \frac{F(t)}{m}\,; \quad (1)$$

here x – deviation of the tuning fork leg from equilibrium position in presence of the excitatory force $F(t) = F_0 \cos\omega t$, ω_0 is resonance frequency of the tuning fork, $\gamma = 2\pi\Delta f$ is attenuation and Δf is the width of the resonance line. Here m being effective mass of tuning prongs and μx^3 accounts the nonlinear behavior of the oscillator with μ being the coefficient of nonlinearity. This term leads to a resonant frequency shift compared to ω_0. Moreover, depending on the sign of μ, the resonance frequency of the oscillations is shifted toward higher or lower frequencies.

In this paper, for the analysis and adjusting of experimental data we apply the Eq. (1), which provides almost the same results as the more general equation [5], but at the same time is more convenient in calculations. The aim of the analysis is finding out the connection between the nonlinear mode of oscillation of the tuning fork prongs and the change in the dependence of the velocity of oscillation on the excitatory force. The aim of actual work is the establishment and research of such a connection, as well as the clarification of the possible influence of the nonlinear force of mutual friction in the superfluid fluid on the nonlinear behavior of the resonator - quartz tuning fork.

Measurement procedure and experimental results

We used a miniature quartz tuning fork, kindly provided to us by the laboratory of Lancaster University, with a resonant frequency in the vacuum of *24983.72 Hz*, length of the leg is $1{,}8\cdot10^{-3}$ *m*, thickness and width of the legs are *75* and *90 mkm*, respectively. The cell and the measurement procedure were previously described in detail [3,6,7]. The studies were made with the solution fridge working at two operating regimes. In one of them we pumped out ^{4}He from a one-Kelvin bath whereas a working solution was condensed in the solution refrigerator. This mode was used to determine the constant of the tuning fork in the experimental cell cooled down to $T = 1.4$ *K*. In other measuring mode the solution fridge worked providing the temperature of the cell and the test fluid of 140 ± 1 *m*K.

The resistance thermometers of RuO_2 were used to determine the temperature. They were placed on the plate of the dissolution chamber and directly in the fluid under study. The thermometers were calibrated using a crystallization thermometer based on the pressure measurement along the ^{3}He melting curve. The accuracy of the measurement and temperature stabilization was ± 1 *mK* being provided by the heater connected by the feedback with the resistance sensor CryoBridge S72A.

In the beginning of the experiment, we measured the quartz tuning fork frequency in a vacuum under different excitatory forces and $T = 1.4$ *K*. Sine-wave constant amplitude U, which is fed from the generator to one of the electrodes of the tuning legs, set the magnitude of the excitatory force, which was determined as $F_0 = aU/2$. On the other electrode, the frequency dependence of the amplitude of the ac current I was measured. This quantity is connected with the oscillation velocity of the tuning legs υ as $\upsilon = I/a$. The piezoelectric constant of the tuning fork was determined from the AFC measured in a vacuum [6].

In Fig. 1 we show typical AFC for a tuning fork in a vacuum obtained with different excitatory forces.

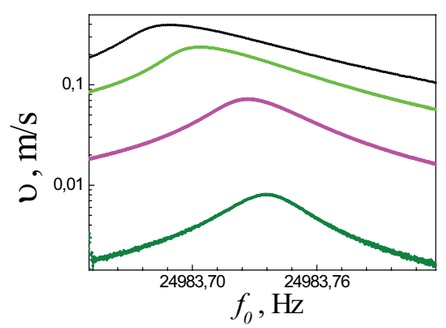

Fig. 1. Velocity of the oscillation of tuning legs in vacuum at different excitatory forces, bottom-up: $1{,}51\cdot10^{-11}$, $1{,}51\cdot10^{-10}$; $6{,}05\cdot10^{-10}$; $1{,}21\cdot10^{-9}$ N. [6].

It is clearly seen in Fig. 1 that at high excitatory forces and, consequently, high voltage amplitudes U one observes a nonlinear oscillation regime that manifests itself in the deformation of the form of the frequency response. Also the resonance frequency decreases with an increase in the excitatory force. Maximum excitatory force in Fig. 1 is $1{,}29 \cdot 10^{-9}$ N, while the oscillation velocity in the resonance maximum was *0.4 m/s*, and the resonance frequency was decreased by *0.048 Hz* comparing with the value at the minimum excitory force. After measuring in vacuum, the solution refrigerator was cooled down to $T < 1$ *K*, to study the flows in ^{4}He. Passing through the nitrogen trap, helium traps and filling capillary, helium attained the experimental cell and condensed there.

Experimental dependences of the oscillation velocity of the tuning fork legs in presence of the excitatory force at temperature of *140 mK*, obtained in various experiments, are shown in Fig. 2. As is seen in Fig. 2, at oscillation velocities $\upsilon \geq 0.046$ *m/s* one observes a noticeable deviation from the linear dependence $\upsilon(F_0)$ shown by the solid line. As was suggested in Ref. 6, this deviation may be explained by the appearance of an additional frictional force that arises due to an increase of the density of quantum vortices and the scattering of thermal excitations - phonons - on their cores (mutual friction) [8]. The flow of helium characterized by the deviation the dependence $\upsilon(F_0)$ from the linear one was called a quasi-laminar in the work [6]. This flow is characterized by the above-mentioned new dissipative mechanism [8].

The force of mutual friction is proportional to the cube of the velocity of the legs: $F_0 \sim \upsilon^3$, which is typical for a turbulent flow (dotted line in Fig. 2). As a result, the total friction force has the form $F_0 = \lambda_q \upsilon + n\upsilon^3$ (solid and dotted lines) [3, 6] where $\lambda_q = 1.32 \cdot 10^{-9}$ *kg/s* and $n = 4{,}62 \cdot 10^{-8}$ *kg·s/m*^{2}, and well describes the experimental data. At the experimental temperature of *140 mK*, the first term, as shown in Ref. 3, is completely determined by the force of friction in the quartz tuning fork material and is due to the bending oscillations of its prongs.

All the amplitudes of the oscillation velocity were measured at the maximum of the resonance curves. At the same time, the resonance curves, at increase in the excitatory force, are deformed due to a nonlinear additional frictional force. In this connection, in [3, 6], we were to analyze the types of AFC curves in the quasi-laminar flow regime. It was shown that the dependence $\upsilon(F_0)$ of Fig. 2 may be conveniently divided into five ranges characterized by a specific type of AFC (characteristic AFCs for each range are given in the works [3, 6]): (I) – region of laminar potential flow He II. Characteristic AFC of this region is shown in Fig. 1 of Ref. 3 and is approximated by Lorentzian. AFC for region II is shown in Fig. 2a of Ref. 3. As was noted, this region is characterized by spontaneous jumps between laminar potential and turbulent currents. Region III was previously depicted in Ref. 6 in Fig. 3 and is characterized by the fact that the AFC starts to be asymmetric relatively the maximum of the resonance curve, and there is a "collapse" towards the lower frequencies. The asymmetry of the AFC curve increases with increasing applied excitatory force until the instability does appear on the resonance curve, being the characteristic feature of the nonlinear behavior of the oscillating body. It should be emphasized that in the region III, regardless of the measurement conditions, one observes both quasi-laminar and turbulent flows. Fig. 3 of present paper and work [6] shows the AFC, measured at a stable quasi-laminar flow regime without the transition to turbulence.

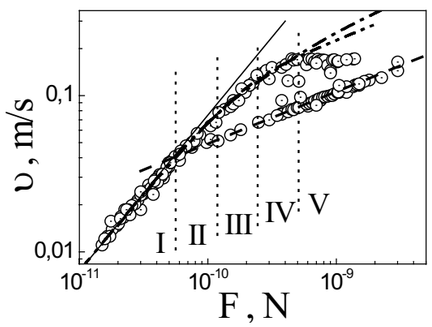

Fig. 2. Dependence of the oscillation velocity of the tuning fork legs on the excitatory force at $T = 140$ *мК*. Solid line is linear dependence $\upsilon \sim F_0$. Dotted line is for turbulent flow mode ($\upsilon^3 \sim F_0$), dot-dash line is calculation accounting the force of mutual friction [3]. Bar-dashed dotted line is the calculation based on the solution of the non-linear Duffing equation, described below in the text.

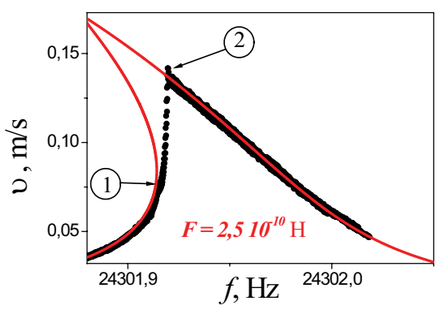

Fig. 3. Amplitude-frequency characteristic of tuning fork for region III with excitatory force $F_0 = 2{,}5 \cdot 10^{-10}$ *N*. Solid curve - calculation using non-linear Duffing equation. 1 and 2 are the points of the beginning and end of the instability on the resonance curve.

In the regions IV and V, the shapes of the resonance curves are qualitatively identical, and in these regions the breakdown in the turbulent flow was observed, in each of the experiments carried out, in the form of a sharp decrease - a jump from the quasi-laminar to turbulent flow. For region IV the curve is shown in Fig. 2b of Ref. 3 and for area V - in Fig. 4 of Ref. 6. As can be seen in Fig. 4 of Ref. 6, in the region V the shape of the resonance curve is strongly deformed in comparison with Lorentzian, and in Fig. 2 it is evident that at the maximum of AFC, the velocity of oscillation of the tuning legs ceases to depend on the applied force.

The fact that the nonlinearity of the oscillation of the tuning fork legs in the regions II-V arises, probably, because of the appearance of an additional nonlinear force of mutual friction in He II, is supported by the measurements made in vacuum. When measured in a vacuum, the amplitude of the velocity was almost three times higher than that at the maximum amplitude of oscillation in He II (see Fig. 1), but there was no markedly expressed nonlinearities of oscillations (deformation of the form of AFC). Thus, it can be argued that the nonlinearity of the oscillations of the tuning fork legs observed in He II, is due to the nonlinear friction force in the liquid, in which the tuning fork is immersed. A similar conclusion was made in the work [2].

Results and discussion

As was noted above and as was shown in Fig. 2 of Ref. 3, as well as in Figs. 3 and 4 of this work, an increase in the excitatory force causing the oscillation of the legs of the tuning fork, leads to the nonlinearity of oscillations, which manifests itself in the deformation of the shape of the AFC until the appearance of instability of the oscillations and reduction of their resonance frequency. To describe these effects, we solve the equation (1) with respect to the modulus of amplitude of the oscillation velocity υ. The result is

$$\upsilon = \frac{F_0}{m} \frac{\omega}{\sqrt{\left(\omega_V^2 - \omega^2 - \omega b \upsilon^2\right)^2 + \omega^2 \gamma^2}}; \quad (2)$$

where ω_V and ω are the resonance frequency of the tuning fork in the vacuum and the current frequency, respectively, $b\upsilon^2$ is the factor which, according to [5], is proportional to the square of the amplitude of the oscillation velocity and the coefficient b is connected with the coefficient of nonlinearity in Eq. (1) by the relation $\mu = \frac{2}{3}\omega_0^3 b$.

The dependence of the velocity on the frequency of nonlinear oscillations calculated by Eq. (2), is shown in Fig. 4 using a constant value $b = 40$ *s/cm*^{2}, which, as will be shown later, is close to the average value in all the experiments carried out. It can be seen that even for low excitatory forces the frequency dependence of velocity demonstrates a slight asymmetry caused by the nonlinearity of oscillations (dashed line, $F_0 = 1{,}5 \cdot 10^{-10}$ *N*). With the increase in the excitatory force, the velocity also increases, and the nonlinearity of oscillations is expressed more and more (a dashed-and dotted curve for $F_0 = 3 \cdot 10^{-10}$ *N*), which leads to a decrease in the resonance frequency and the appearance of instability (points 1 and 3). Instability appears at point 1 if one moves from the left to the right towards to point 1, further movement in frequency continues to the right from the point 2. When moving in frequency in the opposite direction, i. e. from the right to the left, instability, as one might expect, should appear at point 3, with further motion towards lower frequencies from point 4 (hysteresis). However as it was shown in Ref. 2, the measurement of AFC when moving from high frequencies to lower ones and back, give practically identical result. The reason for this is unclear and additional research is needed to clarify the problem. It can be assumed that the nonlinear behavior of the system tuning fork - superfluid is described by the nonlinear term in (2), which origin is mainly connected with the fluid and processes in it. If the nonlinear behavior is related with the properties of the tuning fork itself, then instability at point 3 of Fig. 4 with decreasing frequency would be observed.

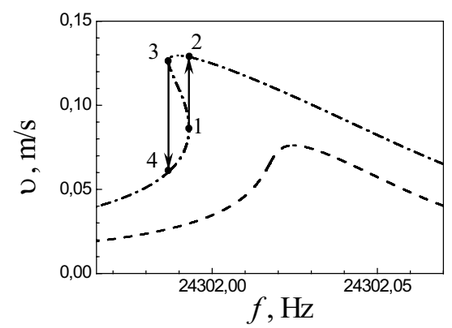

Fig. 4. Amplitude-frequency characteristics, calculated using Eq. (2): dashed line - calculation for $F_0 = 1{,}5 \cdot 10^{-10}$ *N* and $b = 40$ *s/cm*^{2}; dashed-and-dotted line - for $F_0 = 3 \cdot 10^{-10}$ *N* and $b = 40$ *s/sm*^{2}. Arrows show the jumps of the amplitude of oscillations in the event of instability.

It should also be noted that the value of b in Eq. (2) strongly affects the form of the frequency response of velocity, which is determined by this equation. Value of b was estimated by comparing the calculated dependence with the experimental data for the AFC, measured at different excitatory forces for the corresponding experimental data ω_V, ω, γ, m and F_0. The b is the only adjustable parameter. Thus, selecting the value of the coefficient b one can attach the agreement with experimentally obtained resonance curves. Solid lines in Fig. 3 is the result of such calculations.

Note also that at excitatory forces corresponding to the regions II, III, and IV, the resonance curves are well described completely, and for the excitatory forces of the region V, the coefficient b was determined from the part of the curve to the left of point 1. In this frequency range, when the instability finished at point 1 of Fig. 4 of Ref. 6, the velocity value was always below than that at point 2 of Fig. 4 and did not coincide with the values corresponding to the right side of the calculated resonance curve. One should remember that, as it follows from the Fig. 2, the velocity at point 2 of region V is practically constant being and does not depending on the force.

The obtained values of b are shown in Fig. 5 for AFCs which are the result of all measurements. Interval of the excitatory force in Fig. 6 corresponds to the range of values of the excitatory forces in Fig. 2. The figure clearly shows that there is a huge scatter of the values of b. The solid line corresponds to the root-mean-squared value in the studied range, the mean value of the coefficient of nonlinearity coefficient μ is $9.2 \cdot 10^{16}$ $s^{-2}m^{-2}$. At the same time the measurement accuracy of the frequency strongly affects the value of b. The nonlinearity coefficient can also be determined from the data of Ref. 3 presented as $\mu = n\left(\omega_0^3/m\right)$. In this case $\mu = 2{,}5 \cdot 10^{16}$ $s^{-2}m^{-2}$ which is more than three times less than the above value obtained in the actual article. Such a noticeable difference between our values of μ and those of Ref. 3 may be attributed to the fact that the dependence of the damping coefficient γ on the geometry of the problem was not taken into account in Ref. 6.

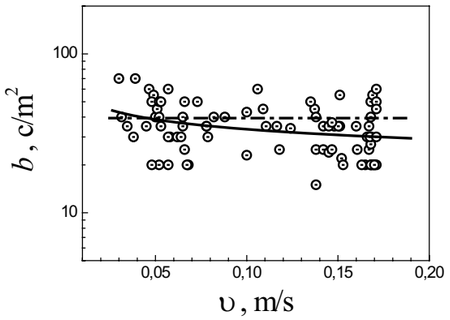

Fig. 5. The values of b, determined from the experimental data on the dependence of the velocity of oscillations on the excitatory force using the non-linear Duffing equation. The solid line is the average value throughout the range of exciting forces. The dotted line is done for $b = 50$ s/m^2.

To determine the effect of the excitatory force on the amplitude of the velocity of the tuning fork prongs in the nonlinear regime, using the Eq. (2), the frequency dependences of velocity were calculated for different excitatory stresses and forces. The value of the velocity corresponding to the end of the instability was determined - point 2 in Figs. 3 and 4, corresponding to the maximum velocity. For low excitatory forces, if the instability was absent (regions I and II), the velocity was taken at the maximum at the resonance frequency of the frequency dependence of velocity. Thus, the dependence $\upsilon(F_0)$ was obtained allowing comparison with experimental data. The best agreement between the estimated and experimental data was achieved at $b = 50$ s/m^2, calculation is shown in Fig. 2 by bar-dashed-and-dotted line. Dot-dash line on Fig. 2 shows the dependence accounting the contribution of mutual friction force, cubic in velocity, in addition to the linear contribution [3], the dotted line corresponds to the turbulent flow when $F_0 \sim \upsilon^3$. As is seen from the figure, when considering the nonlinearity of oscillations (deformation of the shape of the resonance curve), the amplitude of the velocity is a nonlinear function of the applied force. One observes also a rather good agreement between experimental data and the calculation made using the Duffing equation (bar-dashed dotted line in Fig. 2). Note that mean value is within the scatter of the values of b. Thus, one concludes that the experimental data in Fig. 2 can be described both with the solution of the Duffing equation (1), and with the consideration of the cubic term in the expression for the force of mutual friction.

Experimental data indicate that the velocity does not depend on the excitatory force in the region V with relatively high these forces (see Fig. 2). The frequency dependence using the Duffing equation can be described only to the left from the point 1 of the beginning of instability (see Fig. 4).

Conclusions

In present paper, the study is carried out of nonlinear phenomena accompanying the oscillations of a quartz tuning fork, submerged in superfluid helium. The nonlinearity of the oscillations of the tuning fork legs is manifested by the deformation of the shape of the resonance curve for the amplitude-frequency characteristic of the tuning fork. It is shown that the nonlinear frequency response is well described using the Duffing equation for a nonlinear oscillator, by which the dependence of the oscillation velocity of the legs on the excitatory force is treated. It is shown that the same dependence can be obtained by adding a term, cubic in velocity, to the expression for the mutual friction force in the quasi-laminar flow regime. This term is due to the scattering of phonons by quantized vortices of He II, whose density increases with increasing velocity of oscillations. In addition, such a behavior may also indicate an increase in the attached mass or a decrease in the plasticity of the tuning fork due to the appearance of quantum vortices fixed to the surface of the quartz tuning fork.

Thus, the results of our research indicate that the nonlinearity of the tuning fork oscillations is mainly due to the dissipative processes in the superfluid fluid, in which the tuning fork oscillated, which is accompanied by the appearance of a nonlinear term in the dependence of the velocity of oscillations on the excitatory force.

The authors thank E. Ya. Rudavsky for useful discussions. We are also grateful to the ultra-low temperature group from the University of Lancaster (UK) for the quartz tuning fork. The research was partially supported by the research project of youth scientists of the National Academy of Sciences of Ukraine (№ 2/H-2017).

References

1. I.A Gritsenko, G.A. Sheshin, FNT 40, 1028 (2014) [Low Temp. Phys. 40, 802 (2014)].
2. D. Schmoranzer, M. J. Jackson, V. Tsepelin, M. Poole, A. J. Woods, M. Človečko, and l. Skrbek, Phys. Rev. B 94, 214503 (2016).
3. I.A. Gritsenko, K.A. Mykhailenko , S.S. Sokolov, G.A. Sheshin, FNT 42, 215 (2016) [Low Temp. Phys. 42, 163 (2016)].
4. L.D. Landau, I.M. Lifshic Theoretical physics, Mechanics V1, Moscow Pub. “Science” (1988).
5. Astahov V.V. Duffing Oscillator: Textbook for university students [Electronic resource] / V.V. Astahov, S.A. Koblyanskii, A.V. Shabunin – Ed. Saratov University, 2007, 52p. – Access mode: http://chaos.sgu.ru/inno_project/2007/1283/OscDuff-Finish-vers.pdf.
6. I.A. Gritsenko, K.A. Mykhailenko , S.S. Sokolov, G.A. Sheshin, FNT 44, 46 (2018) [Low Temp. Phys. 44, (2018)].
7. I.A. Gritsenko, K.A. Klokol, S.S. Sokolov, G.A. Sheshin, FNT 42, 28 (2016) [Low Temp. Phys. 42, 21 (2016)].
8. E.B. Sonin, Phys.Rev. B 55, 485 (1997).

Вісник ХНУ, серія «Фізика», вип. 29, 2018. с. 22-28

PACS: 05.45.−a
УДК: 53.01/.09

Topological methods in measurement and research of nonlinear dynamical systems

Yu.S. Kurskoy, Yu.P. Machekhin, A.S. Gnatenko

Kharkov National University of Radioelectronics, Nauki Av., 14, Kharkov, 61166, Ukraine

The authors substantiate the need to create a special theory of measurement and analysis of measurement results for nonlinear dynamical systems. The theory should be based on the principles of the open systems theory, dynamic chaos theory and synergetics theory. The authors analyzed the main topological methods and tools for studying of nonlinear dynamic systems. The main characteristics of nonlinear dynamical systems (interval values of dynamic variables, strong dependence on initial conditions and noise, complex, often chaotic dynamics, evolution) were systematized. It was proposed the next topological tools for analysis of measurement results in nonlinear dynamical systems: measurement portrait, Shennon entropy, fractal dimension, forecasting time.

Keywords: nonlinear dynamical system; topology; chaos; Shannon entropy; fractal dimension.

Авторами обґрунтовано необхідність створення спеціальної теорії вимірювання та аналізу результатів вимірювання в нелінійних динамічних системах. Теорія повинна ґрунтуватися на принципах теорії відкритих систем, динамічного хаосу, синергетики. Авторами виконано аналіз топологічних методів та інструментів дослідження нелінійних динамічних систем. Систематизовані основні характеристики нелінійних динамічних систем, серед яких: інтервальність значень динамічних змінних, сильна залежність від початкових умов і шумів, складна, часто хаотична динаміка, еволюція, Запропоновано інструменти аналізу результатів вимірювання: портрет вимірювання, ентропія Шеннона, фрактальна розмірність, час передбачуваності.

Ключові слова: нелінійна динамічна система; топологія; хаос; ентропія Шеннона; фрактальна розмірність.

Авторами обоснована необходимость создания специальной теории измерения и анализа результатов измерения в нелинейных динамических системах. Теория должна основываться на принципах теории открытых систем, динамического хаоса, синергетики. Авторами выполнен анализ топологических методов и инструментов исследования нелинейных динамических систем. Систематизированы основные характеристики нелинейных динамических систем, среди которых: интервальность значений динамических переменных, сильная зависимость от начальных условий и шумов, сложная, часто хаотическая динамика, эволюция, Предложены топологические инструменты анализа результатов измерения динамических переменных нелинейных динамических систем: портрет измерения, энтропия Шеннона, фрактальная размерность, время предсказуемости.

Ключевые слова: нелинейная динамическая система; топология; хаос; энтропия Шеннона; фрактальная размерность.

Introduction.

One of the most important scientific tasks today is a study of the self-organization processes and complex hierarchical systems. They talk about research, forecast and management of characteristics: climate, ecosystems, biopopulations, physical devices (such as a laser) and living organisms (such as a human). All of these objects are classified as open nonlinear dynamic systems (NDS). Their general characteristics include: the nonlinearity of dynamics, strong dependence on the initial conditions and external influences, possibility of chaotic behavior and self-organization. Studies of nonlinear processes and systems are devoted to the works of A.N. Kolmogorov, E. Lorentz, S. Smale, I. Prigogine, H. Haken, V.L. Ginzburg et al. [1-6].

For research, forecast and management of NDS we must create the new methods for experimental research and measurement. Despite the urgency of the issue, the problem of measuring the NDS characteristics until recently was not considered. The authors pointed out the discrepancy between the physical and mathematical foundations of the deterministic classical measurement theory and the processes in NDS [10-12]. For research and measurement in NDS we develop the special measurement theory (Nonlinear Metrology) [10]. It is based on the principles of the next interdisciplinary theories: the information theory, open systems theory, dynamic chaos theory, synergetic theory, and a number of others.

The task of this paper is to make a classification of the dynamical systems, to study their common

https://doi.org/

characteristics, that are important for measurement, and to choose the mathematical methods and tools for analysis of measurement results and forecast the dynamics of complex systems.

1. Classification of the dynamical systems.

A dynamical system is any object (a set of objects) or process (a set of processes). For them the concept of a state is unambiguously defined as a set of the quantities values $[X_1(t),..., X_n(t)]$ at any time t and the law of evolution $F(X_i, t)$ of the initial state $[X_1(t_0),..., X_n(t_0)]$ is given:

$$F[X_1(t_0),..., X_n(t_0)] \to [X_1(t),..., X_n(t)]. \quad (1)$$

A dynamical system can be described by a differential equation of the next form:

$$\frac{dX_i(t)}{dt} = F[X_1(t),..., X_n(t)]. \quad (2)$$

The space of all possible states of the system described by expression (1) forms a phase space. The dimension of phase space, as well as of the system dimension, is determined by number of the dynamic variables $X_i(t)$ (DV).

The dynamic systems include the systems of any nature: physical, chemical and biological objects, societies and populations, ecosystems and financial markets, computing processes and information transformation processes [13]. Classification of dynamic systems can be made based on the nature of origin and the basic properties of the systems.

By the nature of origin, the dynamical systems can be classified as: physical, chemical, biological, information and other systems. By the basic properties, their classification can be performed on the following grounds:

- by nature of dynamics - deterministic, stochastic and chaotic, linear and nonlinear systems;
- by interaction with an external environment - open and closed systems:
- by possibility to converse an energy into a heat - dissipative and conservative systems;
- by the nature of a state change - continuous and discrete systems;
- by possibility of self-organization - evolving and not-evolving systems;
- by structure - single-level and multi-level, complex hierarchical systems.

Let's consider the main features of these systems. Deterministic systems are the systems whose DPs change over time according to a strictly defined law $F(X_i, t)$. Stochastic systems are characterized by the random DVs behavior, the values of which can be described by the mathematical apparatus of probability theory. Chaotic systems are the systems with a chaotic dynamics. Linear systems are the systems with a linear or linearized law of evolution $F(X_i, t)$. Nonlinear dynamical systems are the systems whose evolutionary law can't be described by a linear or linearized equation. The values of NDS DVs change in a nonlinear way. Moreover, the evolution law $F(X_i, t)$ of real NDS can be described analytically extremely rarely. Therefore, as a rule, we can't to make a long-term predication of the NDS state. We should to note that a linear system is also deterministic system, but a nonlinear system, because of complex dynamic, can't be referred to either deterministic or stochastic systems. It can be classified as a partially deterministic system.

Open systems, according to I. Prigogine, are the systems through which the flows of energy and entropy can flow [4]. In case of the large flows, the nonlinear self-organization (evolution) processes can take place in such systems. They are characterized by the spontaneous appearance of a complex, often chaotic, structure. Closed systems, respectively, have properties that are opposite to open ones.

Dissipative systems are the open systems that operate far from the thermodynamic equilibrium and are characterized by the possibility of dissipation (dissipation) of energy coming from outside. Conservative systems are the systems with conservation of energy.

Continuous and discrete systems are characterized by a continuous or discrete, respectively, character of the DVs values change. But in the case of discrete measurement even the continuous systems are considered as the discrete ones.

Evolutionary systems are the systems with the evolution and self-organization functions, which are expressed in decreasing of entropy and increasing of order. A distinctive feature of a hierarchical, complex system is a multilevel structure, each level of which includes the interconnected subsystems.

This classification is incomplete. In a number of publications we can find such types of systems as concentrated and distributed, autonomous and non-autonomous; self-oscillatory and other systems.

If the object of research can be classified as a linear, closed, conservative and deterministic system that for measurement and evaluate their results we can use the methods and tools of the classical measurement theory. The cornerstones of it are: the principle of the existence of the single value of the measured quantity, the satisfaction of the measurement results with the central limit theorem and correctness of the ergodic hypothesis [14]. The nonlinear, dissipative, chaotic, evolutionary systems require a fundamentally different approach to the measurement [15].

The most difficult objects for the research, correct measurement and mathematical description are the open,

dissipative, hierarchical NDS with the chaotic dynamic and self-organization possess. Such systems include the laser, human, ocean and other complex systems. At the same time, the study of chaotic processes in dissipative NDS is one of the fundamental tasks of modern natural science. DVs of such systems are characterized by interval values, the central limit theorem is not satisfied, the ergodic hypothesis is not always confirmed. Dynamic variables must be correctly measured using the measurement models and approaches that are maximum appropriate to the properties and processes in NDS. A correct measurement of the NDS DVs is an obligatory condition for the estimation of current status but allow us to forecast and manage the real systems.

2. Methods and tools for NDS research.

For NDS research it was created a number of interdisciplinary theories. The brightest of they are: the theory of dynamic chaos [13], synergetics [5], theory of dynamical systems [12]. They solve problems of research, modeling and forecasting of the NDS dynamics. Their methods are widely used in applied problems of the broadest direction - from laser engineering to arrhythmology and neurodynamics [16, 17]. The analysis of the main provisions and tools of these theories will allow us to construct a new theory for measurement of the NDS DVs.

The researchers apply two methods for NDS study, that are differed in the type of mathematical model [12]. The first method is based on the mathematical modeling of a system and searching of the evolution function $F(X_i, t)$ (2). The state of the system at the time is a point in the phase space, given by the DVs values $[X_1(t),..., X_n(t)]$ and evolution function $F(X_i, t)$. The system state change corresponds with the movement of the "depicting" point, which describes the phase trajectory. A set of phase trajectories forms a phase portrait of a system. The phase portrait and evolution function make up the mathematical model of a system. The phase portrait serves as an object for studying the dynamics. The evolution function allows us to predict the DVs values. The problem of the described method is a complex mathematical problem of searching of the evolution function $F(X_i, t)$.

The second method focuses on the functional side of a system. It does not allow us to study all features of the internal structure of a system. The system is interpreted as a "black box" with input $[X_1(t_0),..., X_n(t_0)]$ and output $[X_1(t),..., X_n(t)]$ the DVs values. In this case, the "black box" plays the role of the evolution function, transforming the inputs into the outputs, and the mathematical model is determined by the spaces of the inputs and outputs.

The first method has comprehensive information about a system, but in a practice it can be implemented only in rare cases. The second method does not allow us to investigate all the features of a system, but it allow us to determine the DVs values at the time intervals and to construct an incomplete, discrete phase portrait. We think that the second method is most suitable for constructing the models for measurement in the real NDSs.

2.1. Phase portrait.

A phase portrait is the most popular tool of the qualitative theory of dynamical systems [18]. The researching of it allows us to know: the type of system dynamics (deterministic, stochastic or chaotic), Lyapunov exponents, forecast time et al [13]. The values of the system states can be represented by a matrix of dimension $n \times m$ (here n is the number of DVs and m is the number of DVs measurements) in the next form:

$$\begin{vmatrix} X_1(t_0) \dots X_n(t_0) \\ \dots \\ X_1(t_m) \dots X_n(t_m) \end{vmatrix}. \qquad (3)$$

A phase portrait can be limited and unlimited in space, can increase or decrease. The phase volume of the conservative systems is conserved but the phase volume of the dissipative systems is not.

A special kind of a phase portrait is an attractor. It is the state of the dynamical system to which a system aspires in the time during their development. The presence of an attractor indicates a "special" dynamics of a system. There is a strange attractor witch often is a testament of the chaotic dynamics of NDS. Its distinguishing feature is the exponential instability, which is expressed in the exponential discrepancy of the phase portrait trajectories and the fractal dimension [13].

The analysis of a phase portrait is often used in the applied researches of NDS [17]. In the framework of the nonlinear metrology the authors propose to use the "measurement portrait" instead of the classical measurement equation (model equation). It is a graphical and numerical display of the DVs measurement results DV. The measurement portrait is a phase portrait of the NDS trajectory, constructed with the uncertainties or measurement errors [20]. This approach allows us don't find the evolution function.

2.2. Topology and other characteristics of NDS.

S. Smale linked the topology of a phase space and the dynamics of a system [3]. He abandoned the idea of observation an individual trajectory that requires the solution of the equation (2), and proposed to investigate the integral phase space and its geometric structure. Studies have shown that topological transformations of a phase space are a reflection of the physical processes. Thus, the scattering and loss of energy by a system are expressed in the compression of the phase portrait. Approximately the same phase portraits indicate a similar dynamics of the

systems. If the shape of the phase portrait is accessible to the visual representation, the system can be solved.

The geometric study of the phase portraits allows obtaining such data about NDS as: the nature of the dynamics, time horizon for the DVs values prediction, intervals of the DVs values. We can determine: the attractor volume, Lyapunov exponents, Shannon entropy and Kolmogorov entropy, attractor dimension, and other quantities. We suggest use some of these characteristics for analysis of the measurement results in the case of NDS.

2.2.1. Lyapunov exponents are used for study the dynamics of a system in the vicinity of an arbitrary trajectory. They characterize the degree of stretching and contraction of the phase portrait along the selected phase trajectories. If the two close trajectories $x_i(t)$ and $x_{i+1}(t)$ are chosen so that $x_{i+1}(t) = x_i(t) + \xi(t)$, $\xi(0) = \varepsilon, \varepsilon \to 0$ that the next function:

$$\Xi\left[\xi(0)\right] = \lim_{t\to\infty} \frac{1}{t} \ln\left[\frac{\xi(t)}{\xi(0)}\right] \qquad (4)$$

takes a finite series of the Lyapunov exponents $\{\lambda_i\}, i = 1, 2, ..., n$, the totality of which forms the Lyapunov spectrum [13]. The number of Lyapunov exponents corresponds with the attractor dimension D_A, which can be fractional:

$$D_A = j + \sum_{i=1}^{j} \frac{\lambda_i}{|\lambda_{i+1}|}, \qquad (5)$$

here j is the Lyapunov dimension, it is determined from the expressions:

$$\lambda_1 + \lambda_2 + ... + \lambda_j > 0, \ \lambda_1 + \lambda_2 + ... + \lambda_{j+1} < 0.$$

The total Lyapunov exponent Λ can be considered as an indicator of a stability of a system dynamics. When $\Lambda = 0$ it is Hamiltonian system. It has a stable dynamics, the processes occurring in it can be regarded as deterministic processes, the volume of the phase portrait is unchanged $\Delta V_A = const$. When $\Lambda > 0$ the phase portrait volume is growing $\Delta V_A \uparrow$, the NDS dynamics is chaotic. If $\Lambda < 0$ the phase portrait volume decreases , that typical for the dissipative systems.

2.2.2. Entropy. For topological analysis of the NDS phase portrait the Shannon (*H*-entropy(and the Kolmogorov-Sinay (*K*-entropy) are used. *H*-entropy (or information entropy) is one of the key concepts of the information theory [21]. For a system that can be in the states X_i with probability distribution density $p(X_i)$, Shannon entropy is given by the next formula:

$$H = -\sum_{i=1}^{N} p(X_i) \ln p(X_i). \qquad (6)$$

Entropy is a measure of the order or disorder of the system. According to (6), The Shannon entropy assumes large values when the distribution density $p = p(X_i)$ has the values small. If a number of values *N* is bounded, then the entropy is maximal for the uniform distribution law $H \to \ln N$ for $p(X_i) \to 1/N$. The entropy is minimal $H \to 0$ for the normal distribution law when $p(X_i) \to 1$. The entropy of a strange attractor is higher than the entropy of a regular attractor. The entropy of chaotic and random dynamics is higher than the entropy of an ordered motion. The change of the *H*-entropy values indicates a change in the NDS dynamics.

The using the Kolmogorov entropy allowed us to introduce a rigorous criterion of chaotic, as an unstable by Lyapunov motion with positive metric entropy $K > 0$ [13]. Analyzing the phase portrait of a system, the *K*-entropy is defined as:

$$K = \lim_{\substack{d(0)\to 0 \\ t\to\infty}} \frac{\ln[d(t)/d(0)]}{t}, \qquad (7)$$

here *d(0)*, *d(t)* are the distances between two nearby trajectories at the initial and current time, respectively: $d(t) = |x_2(t) - x_1(t)|$.

According (7) the *K*-entropy characterizes the degree of the trajectories divergence, and the degree of randomness of the system dynamics. It is related to the Lyapunov exponents (4) by the expression:

$$K = \int \sum_{\lambda_i \geq 0} \lambda_i(x) \mathrm{d}\mu. \qquad (8)$$

So when the system has chaotic dinamycs its entropy $K > 0$.

The Shannon entropy, *S*-theorem by Yu. Klimontovich [21], entropy scales, we consider as a tool for estimating of the deviation of a system from an equilibrium state. The entropy analysis was used before in the human health measurement model [23] and for estimating the temperature during the laser cooling of particles [24].

2.2.3. Fractal dimension. Many of the NDS processes have the property of self-similarity or scaling - invariance under multiplicative scale changes. Self-similarity can be strict or approximate. A self-similar object or process looks unchanged when you zoom in or out the scale. Such objects and processes include the Brownian particle motion, turbulent flows, strange attractors, time series of the measurement results [25].

The most striking feature of the objects self-similarity is their unusually fine structure. Such objects B. Mandelbrot called the fractals [26]. The importance of fractals lies in the fact that they are able to model a huge number of objects, phenomena and real-world processes, real NDSs.

The fractals are characterized by Hausdorff (or fractal) dimension D_H, It takes fractional values in the interval $0 < D_H \le 3$. For a fractal curve $1 < D_H < 2$, for a surface $2 < D_H < 3$, a point has dimension $D_H = 0$, for a continuous line $D_H = 1$.

Fractal dimension is used in various practical applications to identify the objects and processes. The special interest is its use for analysis of NDS phase portraits and the measurement results time series $x(t_1),...,x(t_n)$ [27]. For determination of the time series fractal dimension D_H we use the statistical method of the normalized range (R/σ - analysis), derived empirically by P. Hurst [25]. The indicator H_R is associated with D_H by next expression:

$$D_H = 2 - H_R \qquad (9)$$

The Hurst index H_R is determined using the value R/σ, here R is the range between the maximum and minimum values of the increment function $x(i,n)$, the value σ is the standard deviation:

$$R(t) = \max_{1\le i\le m} x(i,n) - \min_{1\le i\le m} x(i,n),$$
$$x(i,n) = \sum_{i=1}^{n} (x_i - \overline{x}) \quad , \qquad (10)$$

here $\overline{x_i}$ is the arithmetic mean of the values $x(t_1),...,x(t_n)$.

The correlation R/σ is related with parameter H_R by formula:

$$R/\sigma = (n/2)^{H_R}. \qquad (11)$$

In [27] the fractal analysis (9)-(11) was used for analyze the dynamics of the laser radiation frequency. The author proposed a fractal scale for evaluating the results of measurements with reference points $D_H = 1$, $D_H = 1{,}5$, $D_H = 2$, separating different dynamics characters. If $D_H = 1$ it means that the dynamics of the system is strictly deterministic. If $D_H = 2$ the system behaves in a regular way, but the spread of the measured results is very large, that doesn't allow us to use the methods for processing of the measurement results. If $D_H = 1{,}5$ the process is random. The dynamics corresponds with Brownian motion with independent (Markov) increments. For analyze of such systems characteristics we can use the statistical methods. In the case when $1 < D_H < 1{,}5$ or $1{,}5 < D_H < 2$ the process is non-Markov, chaotic, persistent and antipersistent, respectively.

The fractal dimension allows us to estimate the trend of the DV dynamics of NDS and can be used to predict its values.

2.2.4. Forecasting time. One of the main and oldest tasks of analyzing systems and time series of DV measurement results has been the task of forecasting their dynamics. In some cases, the purpose of the forecasting is not the value of an individual DV, but forecasting of dynamics and its trend. For this, the fractal analysis (9)-(11) and the fractal scales [27] are applied.

The time interval when we can do the correct forecasting of the system dynamics is called the forecasting time or the forecasting horizon. The forecasting time depends on the degree of determinism of the NDS dynamics (the maximal for a deterministic system and minimal for random and chaotic systems) and metrological possibilities [29].

In the case of chaotic NDS, a weak impact of the initial conditions or a small change in the system parameters cause to unpredictability of the resulting motion in finite time, which J. Lighthill [30] called the "forecasting horizon" (or forecasting time). The forecasting time T_{for} is related to the Lyapunov exponent λ (7) as:

$$T_{for}(\lambda) = \frac{1}{\lambda_{\max}} \log \frac{1}{\varepsilon}, \qquad (12)$$

here λ_{max} is the maximum Lyapunov exponent.

In practice, the forecasting time (12) is often calculated using the next simplified formulas:

$$T_{for}(K) = \frac{1}{K}, T_{for}(\lambda) = \frac{1}{\lambda_{\max}}. \qquad (13)$$

The term "forecasting time" is important for the formulation of the measurement equation (model equation) of DVs. We suggest use this value as the correctness time of the measurement equation for NDS case.

3. Measurement principles for NDS case.

The measurement of the NDS DVs is a multi-factor experiment. The processing of the measurement results in a multifactorial experiment is aimed at obtaining the basic scientific data in the new form of mathematical models and their interpretation. We shouldn't only to calculate the average value of the measured quantity or its dispersion [14]. The theory of nonlinear measurements, measurement and analysis models should correspond with the properties of such systems. Let's consider the important for measurement procedures real NDS properties.

The dynamics of NDS has a complex, non-linear, including chaotic, character. NDS exchanges energy and information with the environment and other systems, it is influenced by external factors. The influence of some factors (and noises) is critical for the system, it is can changes the dynamics from random to regular, chaotic, and vice versa.

The state of the NDS at a time moment t is characterized by the n-dimensional state vector $X[X_1(t),...,X_n(t)]$. The DV $X_i(t)$ value changes in time, but stays in the interval $X_i^{\min} \le X_i \le X_i^{\max}$. This interval is due to the functionality of the system. If the DV value outputs of the interval it means that the system destroys.

The phase portrait of NDS in a chaos state is a strange attractor. The exponential dispersal of the phase trajectories leads to the fact that the measured quantities can take any values in the frame of the attractor. If at the moment of measurement t_0 the DV value X_i is in the interval $[y_i(t_0) - u_i(t_0), y_i(t_0) + u_i(t_0)]$ (here $y_i(t_0), u_i(t_0)$ are the estimation and uncertainty of the X_i measurement result at the time t_0) that in tine the DV value will located in attractor frame $[y_{\min} - u_{\min}, y_{\max} + u_{\max}]$ (here $y_{\min}, y_{\max}, u_{\min}, u_{\max}$ are the estimates and uncertainties of the measurement of the X_i minimum and maximum values):

$$[y_i(t_0) - u_i(t_0), y_i(t_0) + u_i(t_0)] \in$$
$$\in [y_{\min} - u_{\min}, y_{\max} + u_{\max}]. \qquad (14)$$

The next, after t_0 time DV values become predictable within the attractor frame (14).

Systems can evolve, some of them have the self-organization function.

Based on the described properties, the authors offer the next topological tools for analyzing the measurement results for NDS case:

1. the time series of the DVs measurement results (3);
2. a measurement portrait (a phase portrait with the measurement uncertainties), constructed on the measurement results (3);
3. the Lyapunov exponents (4);
4. the Shannon (6) and Kolmogorov entropies (8);
5. a fractal dimension (9)-(11) of the measurement time series (3);
6. a forecasting time (13).

In this case, the all quantities values must contain an error (or uncertainty of the measurement results).

The application the physical approaches, topological mathematical methods and tools of nonlinear metrology makes it possible to provide studies of systems with complex, nonlinear dynamics. The topological methods and tools for measurement result analysis help to evaluate the reliability of the measurement data and give a possibility to predict the NDS dynamics.

Conclusions

1. The classification of dynamic systems by origin and properties is performed. It is shown that the dissipative, nonlinear dynamical systems are the most difficult for research, measurement and forecast.

2. The necessity of creating a special theory of measurement and measurement results analysis for nonlinear dynamical systems is substantiated.

3. The analysis of the main topological methods and tools (including topological methods and tools) for the study of nonlinear dynamical systems is performed:

4. The main characteristics of non-linear dynamical systems are systematized, among them: interval values of the dynamical variables, strong dependence on initial conditions and noises, complex, often chaotic dynamics, evolution,

5. In accordance with the main characteristics of nonlinear dynamical systems, the next topological tools for analyzing the measurement results are proposed: measurement portrait, entropy, fractal dimension, forecasting time.

References

1. A.N. Kolmogorov. DAN USSR, 98, 527 (1954).
2. E. Lorenz. Bulletin of the American Meteorological Society. 50, 345, (1969).
3. S.Smale, Bulletim of the Amer. Math. Soc. 66, 1 (1960).
4. I. Prigogine, Time, Structure and Fluctuations, Nobel Lecture. (1977).
5. H. Haken. The science of structure :synergetics:New York: Van Nostrand Reinhold, (1984), 255 p.
6. V.L. Ginzburg, UFN, 169, 4. 419 (1999).
7. Yu.P. Machekhin, V.A. Single, UMJ, 2, 49 (1996).
8. A.S. Gnatenko, Yu.P. Machekhin, Yu.S. Kurskoy, V.P. Obozna, J. Nano- Electron. Phys. 10 (2), 02033 (2018).
9. Yu.P. Machekhin, Yu.S. Kurskoy, A.S. Gnatenko, Radiotekhnica, 192, 2, 102 (2018).
10. Yu.P. Machekhin, Yu.S. Kurskoy, Fundamentals of Nonlinear Metrology: LAP (2014), 240 c.
11. Yu. Machekhin, Yu. Kurskoy, M&T. 60, 3, 49 (2017).
12. Yu. Neimark. Dynamic Systems and Controlled Processes, Editorial URSS, M. (2010). 336 c.
13. V.Yu. Loskutov. UFN, 177, 989 (2007).
14. P.V. Novitsky, I.A. Zograf, Error estimation of measurement results, Energoatomizdat, Leningrad, (1991), 304 p.
15. Yu.P. Machekhin, Yu.S. Kurskoy, Instruments and Methods of Measurement. 6, 2. 257 (2015).
16. G.G. Akchurin, A.G. Akchurin, Letters in JTP, 31, 10, 76 (2005).
17. A.A. Khadartsev, V.M. Eskov, Therapist, 1. 35 (2015).
18. A.A. Andronov, E.A. Leontovich, I.I. Gordon, A.G. Meier, Qualitative theory of second-order dynamical systems, Nauka, M. (1966), 568 c.
19. N.G. Van Campen. Stochastic processes in physics and chemistry. Vischaya shkola, M. (1990), 376 p.
20. Yu. Machekhin, Yu. Kurskoy, E. Prisich, M&T, 61, 5, 48 (2016).

21. Yu.L. Klimontovich, Letters in JTP, 8, 1412 (1983).
22. Yu. Machekhin, Yu. Kurskoy, Measuring technique, 57. 6. 609 (2014).
23. Yu. Machekhin, Yu. Kurskoy, M&T, 50, 6, 56 (2014).
24. Yu. Machekhin Yu. Kurskoy, M&T, 56, 06, 50 (2015).
25. M. Schroeder, Fractals, chaos, power laws, Regular and chaotic dynamics, Izhevsk, (2001), 316 p.
26. B. Mandelbrot, The Fractal Geometry of Nature, Freeman, San Francisco, (1982), 491 p.
27. Yu. Machekhin, Measurement Techniques. 52. 8. 835 (2009).
28. M. Born, Continuity, determinism, reality, Nauka, M. (1971), 415 p.
29. Yu.A. Kravtsov, UFN, 158, 1, 93 (1989).
30. J. Lighthill, Proc. Roy. Soc. Ser. A. 407. 35 (1986).

Вісник ХНУ, серія «Фізика», вип. 29, 2018. с. 29-34

PACS: 62.20.Fe, 62.20.Hg
УДК: 539.374+669.715

Superplasticity of alloy 01420t with the initial bimodal grain structure

D. E. Milaya[1,2], V. P. Poyda[2], V. V. Bryukhovetskiy[1], A. V. Poyda[1]

[1] *Institute of Electrophysics & Radiation Technologies NAS of Ukraine, Chernyshevskaya St. 28, P.O. Box 8812, Kharkov, Ukraine, 61002*
[2] *V.N. Karazin Kharkov National University, Svoboda Sq. 4, Kharkov, Ukraine, 61022*

The temperature – strain rate conditions of high-temperature structural superplasticity are determined for the 01420T alloy with the initial bimodal structure. The structural state of specimens of alloy 01420T, superplastically deformed to failure under the conditions of high-temperature structural superplasticity, is studied. It is revealed that in the working part of specimens of the alloy 01420T during the superplastic deformation fibrous structures forms as a result of the viscous flow. They are localized in grain boundary cavities and cracks. The probable causes of partial melting of the 01420T alloy and the mechanism of its superplastic deformation are analyzed.
Keywords: superplasticity; grain boundary sliding; structural anisotropy; bimodal structure.

Для сплаву 01420Т з вихідною бімодальною структурою визначені температурно-швидкісні умови прояву високотемпературної структурної надпластичності. Вивчено структурний стан зразків сплаву 01420Т, надпластично продеформованих до руйнування в умовах високотемпературної структурної надпластичності. Виявлено, що в робочій частині зразків сплаву 01420Т при надпластичної деформації утворюються волокнисті структури в результаті в'язкого плину. Вони локалізовані в примежевих порах і тріщинах. Проаналізовано ймовірні причини часткового плавлення сплаву 01420Т і механізм його надпластичної деформації.
Ключові слова: надпластичність; зерномежеве проковзування; структурна анізотропія; бімодальна структура.

Для сплава 01420Т с исходной бимодальной структурой определены температурно-скоростные условия проявления высокотемпературной структурной сверхпластичности. Изучено структурное состояние образцов сплава 01420Т, сверхпластично продеформированных до разрушения в условиях высокотемпературной структурной сверхпластичности. Выявлено, что в рабочей части образцов сплава 01420Т при сверхпластической деформации образуются волокнистые структуры в результате вязкого течения. Они локализованы в приграничных порах и трещинах. Проанализированы вероятные причины частичного плавления сплава 01420Т и механизм его сверхпластической деформации.
Ключевые слова: сверхпластичность; зернограничное проскальзывание; структурная анизотропия; бимодальная структура.

Introduction

It is known that semifinished products of industrial deformable aluminum alloys in the initial state have an inhomogeneous structure [1, 2]. In order for these alloys to exhibit the effect of structural superplasticity (SSP), it is necessary to perform their additional thermomechanical treatment aimed at forming a uniform ultrafine-grained structure. It takes time and additional energy costs. In this connection, it becomes necessary to determine the temperature – strain rate conditions for the development of the SSP for various deformable aluminum alloys that, in the initial state, have a non-uniform grain structure.

The results of experimental studies aimed at determining the temperature – strain rate conditions in which specimens of the 01420T alloy with the initial bimodal structure during their deformation in the creep regime at a constant flow stress show the SSP effect are considered in the article. It also contains data on the structural state of superplastically deformed specimens of this alloy and the concept of their superplastic deformation mechanisms (SPD).

Materials and methods of the experiment

Medium-durable alloy 01420T (5,0-6,0%Mg; 1,9-2,3%Li; 0,09-0,15%Zr; 0,1-0,3%Si; 0,3%Fe; 0,1%Ti; 0,3%Mn; 0,005%Na; base Al, % wt.) has strength limit σ_B = 440-470 MPa [3]. This alloy belongs to the lightest of aluminum-lithium alloys. Its structure is matrix-type. In the 01420T alloy of the Al-Mg-Li system in equilibrium with the matrix phase (α-solid solution on the aluminum base) there are such phases: β (Mg_3Al_3), γ ($Mg_{17}Al_{12}$), δ (AlLi), S_1 ($MgLiAl_2$) [3]. It is found that a stable phase

https://doi.org/

S_1 is predominantly localized at the grain boundaries of the matrix phase, forming them almost continuous [3]. In the body of the matrix phase grains, in addition to the above phases, phase particles δ' (Al_3Li) are also located, which provide hardening of the alloy after artificial aging, as well as dispersed particles of β' ($ZrAl_3$). They are used for stabilization of the grain structure of aluminum alloys at high homological temperatures [1-3].

Mechanical tests of the alloy 01420T specimens with dimensions of the working part of 10 mm and cross section of *3.0-5.0 mm* were performed in air by straining in a creep mode at a constant flow stress in accordance with the procedure detailed in at [4]. The experimental creep curves recorded using a Sanwa PC 500a digital multimeter were rearranged in the coordinates "true strain" - "time" and served to determine the true strain rate $\dot{\varepsilon}_{true}$.

To detect grain boundaries during metallographic studies, a chemical etchant of the following composition was used: *17 ml* of HNO_3, *5 ml* of HF, *78 ml* of H_2O.

The grain structure, cavity morphology, and fibrous structures in the specimens were examined using a light microscope MIM-6 with a Pro-MicroScan digital camera and a scanning electron microscope Tescan VEGA 3 LMH, as well as standard quantitative metallography methods [5].

The average grain size ‹*d*› was determined from microphotos by the method of random secants [5].

To reveal grain boundaries on the surface of the working part of superplastically deformed specimens of the investigated alloy, along with chemical etching, the deformation relief method was used, which was described in [4].

Results and Discussion

As a result of structural studies, it was determined that the initial grain structure of the working part of specimens of the 01420T alloy prepared for mechanical testing is bimodal (Fig.1).

The overwhelming majority of grains that are concentrated in the colony, occupying a large area in the working part of the specimens, are ultra-small. Their average size is approximately *5 μm* (Fig.1, a). In some sections of the working part of the specimens, which have the form of strips (Fig.1, b), the major oblong grains are mainly concentrated (Fig.1, c). They are separated from each other by low-angle boundaries, which are parallel or approximately perpendicular to the strain direction of the specimens. The average size of large polygonized grains is approximately *25 μm*. In the strips, there is also a certain number of equiaxial fine grains, which have high-angle boundaries. Their average size is about *12 μm*. Specimens of the alloy 01420T were deformed in the creep regime at a constant flow stress σ = 2.0-7.0 MPa and a temperature T = 520°C, at which, as was determined in [6], partial melting of the 01420T alloy occurs. It leads to the formation of the local arias of the metastable liquid-solid phase on the grain boundaries.

As a result of the mechanical tests, it was determined that specimens of the 01420T alloy, which had undergone thermomechanical treatment, exhibit the effect of high-

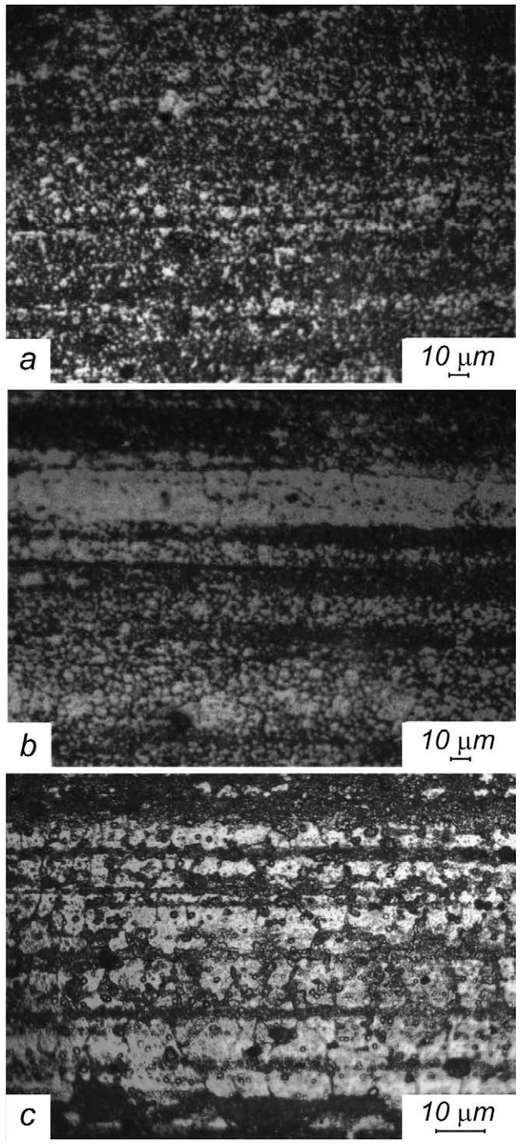

Fig.1. Characteristic types of the initial bimodal microstructure of the working part of specimens of alloy 01420T; a - a colony consisting of ultra-fine grains; b - colony in which large and small grains are concentrated; c - characteristic types of grains which are in the colony, shown in Fig. 1, b. Light microscopy.

temperature SSP. Analysis of creep curves, one of which is shown in Fig.2, showed that they have small areas of unsteady creep and some stages of accelerated creep. The main deformation, which is several hundred percent, specimens of alloy 01420T accumulate, deforming superplastically at the stage of flow, which corresponds to steady creep. It is determined that the values of the true deformation rates of specimens of the alloy 01420T deformed at T = 520°C and flow stresses σ = 2.0-7.0 MPa lie in the range 10^{-3}-10^{-5} s^{-1}.

It is determined that the maximum elongation to failure δ, which is 450%, is observed in specimens superplastically deformed at T = 500°C, σ = 4.5 MPa and the true strain rate $\dot{\varepsilon}_{true}$ = $2.2 \cdot 10^{-3} s^{-1}$. These temperature – strain rate conditions are optimal for the manifestation of the effect of high-temperature SSP of specimens of the investigated 01420T alloy with the initial bimodal structure.

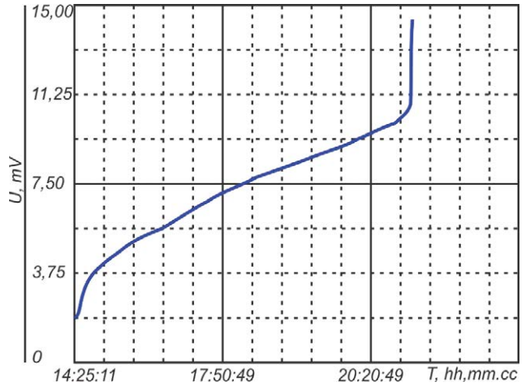

Fig.2. The experimental creep curve of a specimen of the 01420T alloy superplastically deformed to failure under the optimal conditions at T = 520°C and a flow stress σ = 4.5 MPa.

Figure 3 shows a general view of a specimen of the 01420T alloy deformed to failure under the optimum conditions of high-temperature SSP in comparison with the initial one.

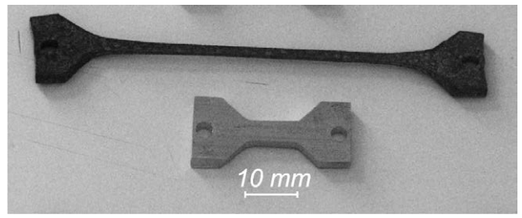

Fig.3. The general view of the specimen of the 01420T alloy deformed to 450% under the optimal conditions of the high-temperature SSP in comparison with the initial one.

It was found that, at a macroscopic level, the superplastic flow of specimens of the 01420T alloy was stable, and their failure occurred without neck formation. Figure 4 shows a characteristic view of the deformation relief formed on the surface of the working part of the specimen of the 01420T alloy deformed to failure under the optimal conditions of the high-temperature SSP. It can be assumed that it arose as a result of the development of grain boundary sliding (GBS), which was intensively carried out along the high-angle boundaries of ultrafine and fine grains with the participation of grain-boundary cavities in accordance with the SPD mechanism proposed in [7], and also on the low-angle boundaries of large grains.

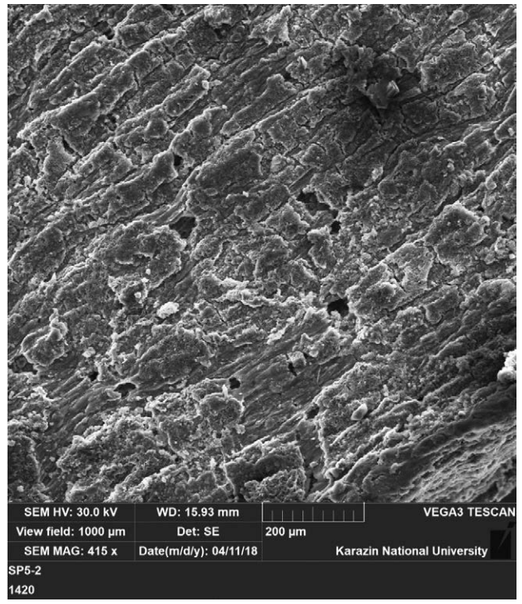

Fig.4. A characteristic view of deformation relief formed on the surface of the working part of the specimen of the 01420T alloy superplastically deformed to failure under the optimal conditions of the high-temperature SSP.

It should be noted that the observed mutual sliding of large polygonized grains occurs through low-angle intergranular boundaries parallel to the strain direction, which is not characteristic for existing classical ideas of the development of GBS under conditions of a micrograin SSP [2]. The GBS of polygonized grains over low-angle boundaries was observed by us earlier in the investigation of the SSP of alloy 1933 [8].

Figure 5 shows the characteristic microstructure of the working part of specimens of the alloy 01420T, superplastically deformed under the optimal conditions to failure, obtained using light microscopy methods. It is determined that as a result of heating the specimens of the alloy 01420T to the test temperature, and also during their

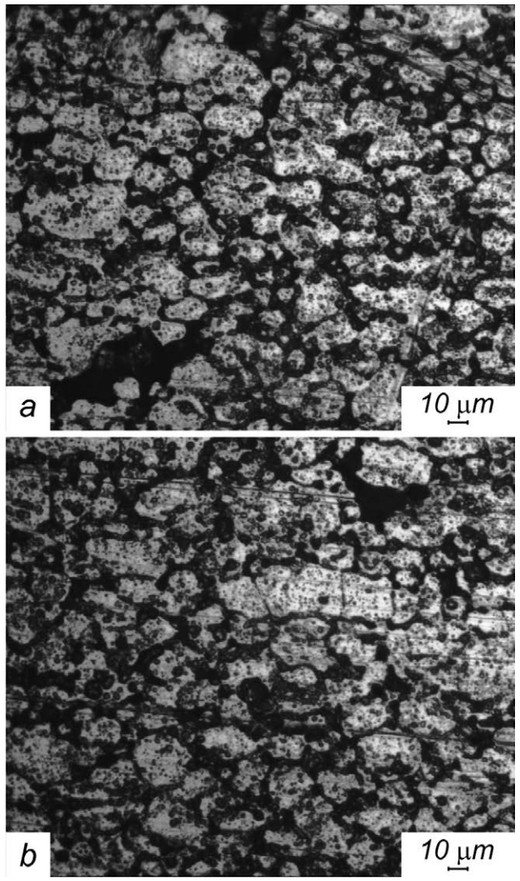

Fig.5. Characteristic types of microstructure of the working part of specimens of alloy 01420T, superplastically deformed to failure under the optimal conditions of high-temperature SSP. Light microscopy. The direction of stretching is horizontal.

SPD, the bimodal structure, due to the development of static and dynamic recrystallization, basically turns into a homogeneous grain structure.

This is evidenced by the absence in the microstructure of the working part of specimens of colonies of grains that have substantially different sizes and shapes (see Fig.5). It was found that the predominant number of grains in the working part of specimens superplastically deformed to failure under the optimal conditions of the SSP is ultra-small. Their average size is about *10 μm*. However, in some of its parts, a few large polygonized grains, separated by low-angle boundaries, have been preserved (see Fig.5, b). Their average size is approximately *20 μm*. In the structure of the alloy there are also fine grains, whose average size is *15 μm*.

It is determined that in the working part of the specimens during their SPD, grain boundary cavities were formed and developed due to the GBS. The average size of cavities is comparable with the average size of the mutually slipping grains adjoining them (see Fig.4 and Fig.5). In the structure of the failured specimens, along with grain-boundary cavities, magisterial cracks formed because of their unification are observed.

As a result of the research of the characteristic types of deformation relief of the specimens of the 01420T alloy working part, fibers were found (see Fig.6), localized in near-surface grain boundaries and microcracks. It is found

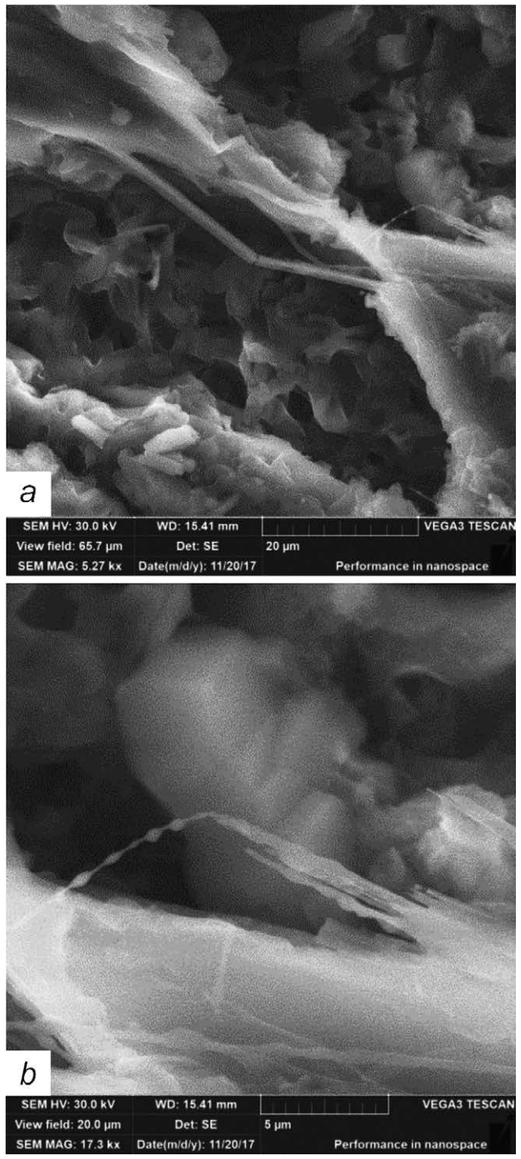

Fig.6. A characteristic type of fibrous structures formed in specimens of the alloy 01420T superplastically deformed to failure under optimal the conditions of the SSP.

that the ends of these fibers are connected to the surface of grain-boundary cavities and cracks formed in the course of GBS when the grains are separated from each other along grain boundaries approximately perpendicular to the extension direction. On some fibers (see Fig.6, b) there are drops. The number of fibers formed in the near-surface grain-boundary cavities is different. Apparently, it depends on the volume of the metastable liquid phase localized at the grain boundaries perpendicular to the strain direction of the specimen.

The presence of fibrous structures and a characteristic form of their morphology indirectly indicate that the SPD of the specimens of the 01420T alloy with the original bimodal structure, as well as of the other multicomponent aluminum alloys alloys [6, 8-16] and observed by other authors [17, 18], takes place with the presence on high-angle and low-angle grain boundaries of viscous metastable liquid-solid phases on some sections.

Let us analyze the probable causes of the formation of a metastable liquid phase in specimens of the 01420T alloy at high homological temperatures, using the ideas that were presented in [6, 8-16, 20, 21].

Apparently, the most probable reason for the formation of a metastable liquid phase in the specimens of the 01420T alloy, which takes place during the heating of specimens to the test temperature T = 520°C and during their SPD at this high homological temperature, is the local melting of the border sections of grains (their "mantle" and those sections of grain boundaries in which the aluminum-based solid solution has an increased concentration of lithium and magnesium atoms in comparison with the nominal composition of the alloy. As is known, the atoms of these elements, which are in the form of segregations at the grain boundaries or dissolved in aluminum-based solid solution to the limiting concentration, significantly reduce the melting temperature of the alloy in the local sections of its specimens [22].

It can also be assumed that a number of particles of the S_1 phase containing magnesium and lithium, dissolve in an aluminum-based α-solid solution during the heating of the specimens to the test temperature due to the development of diffusion processes in the solid state. The particles of the S1 phase remaining at the grain boundaries, which did not have time to dissolve at the time of the start of the SPD of the specimen, the nonequilibrium structural components into which this phase come in, as well as other intermetallide phases containing magnesium and lithium, apparently melt and also are foci of partial melting of the alloy. As a result of its realization, the areas occupied by the metastable liquid phase nucleate on the grain boundaries. The study of the surface of the working part of specimens of alloy 01420T, deformed to failure, showed that it is covered with loose oxide films (see Fig.5). This suggests that in the course of SPD, dynamic oxidation of the surface of solid grains as well as the surface of inclusions of the metastable liquid phase, which was present in small amounts at grain boundaries, intensively took place. Because of this, apparently, the formation of fragile oxide films consisting of Al_2O_3, MgO, and magnesium spinel $MgAl_2O_4$, characteristic for multicomponent aluminum alloys doped with magnesium, occurred [23-25]. It can be assumed that during the SPD, the metastable liquid phase accumulates a certain amount of dispersed particles formed upon the breakdown of loose oxide films. This process apparently leads to the formation of viscous suspensions at grain boundaries of inclusions according to the mechanism described in [27], which consists of a melt of aluminum-based α-solid solution and dispersed particles, which are fragments of oxide films. The resulting liquid-solid phase apparently has an important influence on the development of deformation and accommodation processes occurring during the SPD of specimens of the 01420T alloy.

It can be assumed that in the solid sections of the working part of the specimens of the investigated alloy 01420T during the SPD, such basic deformation mechanisms seem to act simultaneously and self-consistently: GBS, intragranular deformation, diffusion creep. Apparently, at the early stages of superplastic flow of specimens of the 011420T alloy, intragranular deformation, due to slipping and creeping of lattice dislocations, will develop both in large polygonized grains and in those small and ultra-fine grains in which the stresses, in accordance with the Schmid law, reached a critical shear stress. As is known [2], the interaction of lattice dislocations with grain boundaries during SPD is used to create a nonequilibrium state of the high-angle grain boundaries, over which the GBS takes place. It can be assumed that intense GBS on solid sections of the high-angle boundaries of small and ultra-fine grains occurs simultaneously with the viscous flow in those sections of the high-angle boundaries of fine and ultra-fine grains, as well as at low-angle boundaries of large grains parallel to the strain direction, which contain a viscous liquid-solid phase in accordance with the positions of the models described in [20, 21, 27, 28]. The effective accommodation to GBS in this case is due to the development of diffusion processes in the solid and liquid phases, as well as a result of the dislocation sliding in the core of grains and near their boundaries. Because of coordinated implementation of deformation and accommodation processes in the microstructure of the working part of the specimens of the 01420T alloy, an intensive grain rearrangement takes place. It can be assumed that viscous flow of a metastable liquid phase localized at high-angle grain boundaries perpendicular to the strain direction due to the opening of grain-boundary cavities during GBS leads to the formation and development of fibrous structures in the SPD process of specimens of the 01420T alloy in accordance with the mechanism described in [9, 11].

The joint manifestation of all deformation and accommodation mechanisms creates favorable conditions for the stable flow of specimens of the 01420T alloy with the initial bimodal structure and ensures their SPD by hundreds of percent.

Conclusions

1. The temperature – strain rate conditions are determined for which specimens of the 01420T alloy with the initial bimodal structure exhibit the effect of high-temperature structural superplasticity.

2. The structural state of specimens of alloy 01420T, superplastically deformed to failure under conditions of high-temperature structural superplasticity, is studied.

3. It is revealed that in the working part of specimens of the alloy 01420T during the superplastic deformation, as a result of the viscous flow, fibrous structures forms. They are localized in grain boundary cavities and cracks.

4. The probable causes of partial melting of the 01420T alloy and the mechanism of its superplastic deformation are analyzed.

References

1. V.N. Shcherba. Pressovanie alyuminievykh splavov. M.: Intermetinzhiniring, (2001), 768s.
2. O.A. Kaybyshev. Sverkhplastichnost promyshlennykh splavov. M.: Metallurgiya, (1984), 264s.
3. I.N. Fridlyander K.V. Chuistov, A.L. Berezina, N.I. Kolobnev Alyuminiy-litiyevyye splavy. Struktura i svoystva. K: Naukova dumka, (1992), 192 s.
4. V.P. Poyda, R.I. Kuznetsova, T.F. Sukhova, N.K. Tsenev i dr. Metallofizika, T.12, №1, 44 (1990).
5. S.A. Saltykov. Stereometricheskaya metallografiya. M.: Metallurgiya, (1976), 272 s.
6. V.P. Poyda, D.Ye. Milaya, A.V. Poyda, V.V. Bryukhovetskiy, R.V. Sukhov. Voprosy atomnoy nauki i tekhniki. Seriya «Fizika radiatsionnykh povrezhdeniy i radiatsionnoye materialovedeniye», №4 (92). 139 (2014).
7. R.I. Kuznetsova, N.N. Zhukov, O.A. Kaibyshev, R.Z. Valiev. Phys. Stat. Sol., V.70A, N 2, 371 (1982).
8. V.V. Bryukhovetsky, A.V. Poyda, V.P. Poyda, D.E. Milaya. Voprosy atomnoy nauki i tekhniki, seriya «Fizika radiatsionnykh povrezhdeniy i radiatsionnoye materialovedeniye», №2 (114), 94 (2018).
9. V.P. Poyda, V.V. Bryukhovetskiy, R.I. Kuznetsova, A.V. Poyda, V.F. Klepikov. Metallofiz. Noveyshiye Tekhnol., V.25, N1, 117 (2003).
10. A.V. Poyda, V.V. Bryukhovetskiy, D.L. Voronov, R.I. Kuznetsova, V.F. Klepikov. Metallofiz. Noveyshiye Tekhnol., V.27, N3, 319 (2005).
11. V.P. Poida, V.V. Bryukhovetskii, A.V. Poida, R.I. Kuznetsova, V.F. Klepikov, D.L. Voronov. The Physics of Metals and Metallography, V.103, Issue 4, 414 (2007).
12. V.V. Bryukhovetskiy, V.P. Poyda, A.V. Poyda, R.I. Kuznetsova, Kafarani Ali Makhmud, D.Ye. Pedun. The Physics of Metals and Metallography, V.110, №6, 614 (2010).
13. D.Ye. Pedun, V.P. Poyda, V.V. Bryukhovetskiy, A.V. Poyda, A.P. Kryshtal', T.F. Sukhova, A.L. Samsonik, V.V. Litvinenko, Ye.A. Spiridonov, Metallofizika i noveyshiye tekhnologii. V.34, №10, 1397 (2012).
14. D.Ye. Pedun, V.P. Poyda, V.V. Bryukhovetskiy, A.V. Poyda, R.V. Sukhov. Voprosy atomnoy nauki i tekhniki, seriya «Fizika radiatsionnykh povrezhdeniy i radiatsionnoye materialovedeniye», №5(8), 147 (2013).
15. V.P. Poyda, D.Ye. Pedun, V.V. Bryukhovetskiy, A.V. Poyda, R.V. Sukhov, A.L. Samsonik, V.V. Litvinenko. The Physics of Metals and Metallography, V.114, №9. 848 (2013).
16. D.E. Pedun, V.P. Poyda, V.V. Bryukhovetskyy, A.V. Poyda, R.V. Sukhov, A.P. Kryshtal′ Visnyk KHNU, seriya «Fizyka», №1075, V.18, 55 (2013).
17. C.L. Chen, M.J. Tan. Mater. Sci. and Eng. A., 298, 235 (2001).
18. W.D. Cao, X.P. Lu, H. Conrad. Acta. Mater., 44, №2, 697 (1996).
19. V.V. Bryukhovetskiy, A.V. Poyda, V.P. Poyda, Yu.V. Kolomak. The Physics of Metals and Metallography, V.112, №5, 552 (2011).
20. V.V. Bryukhovetskiy, A.V. Poyda, V.P. Poyda, V.F. Klepikov, Yu.V. Kolomak. Voprosy atomnoy nauki i tekhniki, Seriya: Fizika radiatsionnykh povrezhdeniy i radiatsionnoye materialovedeniye, №4. (98), 78 (2011).
21. J. Koike, M. Mabuchi, K. Higashi Acta Met. Mater, V.43, №1, 199 (1995).
22. V.I. Dobatkin, R.M. Gabidullin, B.A. Kolachev, G.S. Makarov M.: Metallurgiya (1976) 264s.
23. M.V. Mal'tsev, Yu.D. Chistyakov, M.I. Tsypin, DAN SSSR, V.49. №5. 813 (1954).
24. I.N. Fridlyander, V.S. Sandler, T.I. Nikol'skaya i dr. Metally, №2, 221 (1978).
25. A.M. Korolkov Liteynyie svoystva metallov i splavov. M.: Nauka, (1967). 199s.
26. M. Mabuchi, K. Higashi. Acta mater, Vol. 47, № 6, 1915 (1999).
27. V.N. Perevezentsev, Yu.V. Svirina. ZhTF, V.68, №12, 38 (1998).

Вісник ХНУ, серія «Фізика», вип. 29, 2018. с. 35-38

PACS:
УДК:

Effect of high hydrostatic pressure on various diffusion mechanisms in oxygen deficient $ReBa_2Cu_3O_{7-x}$ (Re=Y, Ho) single crystals

Yu.I. Boyko, G. Ya. Khadzhai, N. R. Vovk, R. V. Vovk, I.L. Goulatis

V.N. Karazin Kharkov National University, Svoboda Sq. 4, Kharkov, Ukraine, 61022

In present paper the effect of high pressure on the relaxation of the electrical resistivity at room temperature of oxygen nonstoichiometric $ReBa_2Cu_3O_{7-x}$ (Re = Y, Ho) single crystals are investigated. It is established that the hydrostatic pressure significantly intensifies the process of diffusion coalescence in the oxygen subsystem. At the same time, the intensity of the redistribution of labile oxygen significantly changes when yttrium is replaced by holmium.

В работе исследовано влияние высокого давления на релаксацию электросопротивления при комнатной температуре монокристаллов $ReBa_2Cu_3O_{7-x}$ (Re=Y, Ho) нестехиометрического по кислороду состава. Установлено, что гидростатическое давление существенно интенсифицирует процесс диффузионной коалесценции в кислородной подсистеме. При этом интенсивность перераспределения лабильного кислорода существенным образом изменяется при замене иттрия на гольмий.

В работе исследовано влияние высокого давления на релаксацию электросопротивления при комнатной температуре монокристаллов $ReBa_2Cu_3O_{7-x}$ (Re=Y, Ho) нестехиометрического по кислороду состава. Установлено, что гидростатическое давление существенно интенсифицирует процесс диффузионной коалесценции в кислородной подсистеме. При этом интенсивность перераспределения лабильного кислорода существенным образом изменяется при замене иттрия на гольмий.

Introduction

As is well known, the presence of labile oxygen [1,2] in high-temperature compounds (HTSC) $ReB_2Cu_3O_{7-x}$ (Re = Y or other rare earth element) leads to the appearance of a non-equilibrium state that can be manifested during the application of high pressure [3,4], a step by step change in temperature [5,6], long-term storage [7-9], contribute to phase separation processes [10,11], ascending diffusion [12,13] and the appearance of various superstructures [14-16]. All these processes have a significant effect on the physical properties of HTSC in both the normal and superconducting states and are most clearly manifested in the case of oxygen deficient samples [17,18].

The modification of the structural and electrophysical characteristics of superconducting materials can be achieved by applying various external influences [19-21] and is an important experimental tool of modern solid state physics. In particular, the study of the effect of the external hydrostatic pressure [22,23] on the structural state and transport processes in $ReBa_2Cu_3O_{7-x}$ single crystals, is a source of important information necessary for elucidating the microscopic mechanism of "high-temperature" superconductivity, which until now remains unclear [24]. Taking this into account, experimental methods have proved to be of a particular importance, allowing us to reveal the parameters of superconductors, which most significantly affect their physical characteristics in the normal and superconducting states. One of the most important methods is the use of high pressure [25-27], since this not only makes it possible to clarify the role and the influence of structural features of the system on the superconducting states formation, but also enables to model the conductive characteristics and critical parameters of the superconductor.

A characteristic feature of the $YBa_2Cu_3O_{7-x}$ compound is the relative simplicity of the complete or partial substitution of yttrium by its isovalent analogues, which enables the variation of the conductive characteristics, and thereby can verify the adequacy of theoretical models. In this respect, the substitution of yttrium by the holmium, which has a sufficiently large magnetic moment ($10.61\mu_B$ and $9.7\mu_B$ in $HoBa_2Cu_3O_{7-x}$), allows us to predict a qualitatively different behavior of the system due to the paramagnetism of $HoBa_2Cu_3O_{7-x}$ in the normal state [2]. It is of interest to study oxygen deficient samples, in which the rare-earth ion can serve as a sensor sensitive to the local symmetry of its environment and to the distribution

https://doi.org/

of charge density, since their change affects the crystal field that forms the electronic structure of such an ion [6].

In this work, we study the effect of an external hydrostatic pressure up to 5 kbar on the temperature dependence of the electrical resistance $\rho(T)$ in the *ab* plane of $ReBa_2Cu_3O_{7-x}$ (Re = Y, Ho; x≈0.3-0.47) single crystals in the temperature interval from 300 K to the temperature of the superconducting transition T_c.

Experimental methodology

The crystals were grown by the "solution-melt" method in a gold crucible as was previously described [18]. The samples had the shape of a parallelepiped with dimensions $YBa_2Cu_3O_{7-x}$ - 2x1.8x0.5 mm^3 and $HoBa_2Cu_3O_{7-x}$ - 1.9x1.9x0.5 mm^3. The largest area of the sample corresponded to the crystallographic ab plane. Initially, the samples were heat-treated in oxygen flow at T = 400° C for five days to saturate them with oxygen completely, i.e., to reduce the parameter x to a value ≈ 0 – 0.1.

The temperature dependence $\rho(T)$ was first measured during the heating of the multiplier under atmospheric pressure. The pressure was then gradually increased at room temperature. When the desired pressure was reached, the multiplier was cooled to a temperature $T < T_c$, and after that the $\rho(T)$ measurements were carried out. Following the measurement at the maximum pressure, the pressure was lowered to atmospheric pressure and the $\rho(T)$ measurements were repeated.

In addition to the $\rho(T)$ dependence, we carried out isothermal measurements of the change of the electrical resistance ρ at temperature 300 K as a function of time under pressure ≈ 5 kbar, as well as after its removal. In this experiment, the maximum exposure time reached ≈ 80 hours.

Results and discussion

In previous work [29], the results of the electrical resistance time relaxation dependence at room temperature: curve 1 - after the application of pressure 5 kbar and curve 2 - after the pressure released were presented. Thus, it was determined that after the pressure was removed, the equilibrium resistance value was reached much faster than when the pressure is applied. To explain the latter result, we proposed that the observed phenomenon is due to the difference in the diffusion paths of the pressure-induced process of elongation-shortening of oxygen ion chains in Cu-O planes.

Thereafter [6], we provided evidence that the diffusion of oxygen ions in the $ReBa_2Cu_3O_{7-x}$ (Re=Y, Ho) compounds can take place via two mechanisms. At the initial stage of the process, the single-channel diffusion mechanism is dominant, whereas in the final stage the diffusion of oxygen ions is limited by the conventional mechanism of classical diffusion. In the first case, oxygen ion diffusion is characterized by the $\langle L^2\rangle \sim t^{1/2}$ dependence and in the second case by the $\langle L^2\rangle \sim t$ dependence.

The study of the time dependence $\rho=f(T)$ carried out previously [29] (relaxation curves) also indicates that in this case there are two stages: a fast initial stage and a slower final stage. This result can also explain the existence of two mechanisms for the redistribution of oxygen ions induced by the application of pressure. To confirm the correctness of this assumption, we processed these relaxation curves by constructing the $(\rho_0/D\rho)^2=f(T)$ dependences, which, in fact, determine the operation of the one or the other oxygen ions' diffusion mechanism (refer to Figure 1).

Figure 1, in our opinion, confirms the correctness of the previously stated assumption that the application of an external pressure of ~5 kbar causes the diffusion redistribution of oxygen ions in the formation-decay of the oxygen clusters in the $ReBa_2Cu_3O_{7-x}$ (Re = Y, Ho) compounds. Herewith, the diffusion of oxygen ions process is realized by two mechanisms: By the single-channel diffusion mechanism and by the conventional classical diffusion mechanism (at the final stage of the process).

The entire set of the experimental results obtained, agrees well, if presume that the external hydrostatic pressure intensifies the appearance of several (at least two) phases in the studied samples, characterized by different values of the transition temperature Tc. In our opinion this is due to the process of the redistribution of the oxygen ions in the volume of $ReBa_2Cu_3O_{7-x}$ (x=0,4) crystals. The pressure accelerates the diffusion coalescence process [30] of microscopic clusters of various sizes oxygen vacancies formed in the crystal due to the oxygen deficiency. As a result of the coalescence, oxygen ions are redistributed in the crystal, which leads to an increase of a number of sufficiently large in size ordered one-dimensional clusters of oxygen ions. At the same time, the parameter x decreases. Accordingly, the number of specific structural entities - negative U-centers, capable of generating coupled charge carriers [31] increases. In this case, a higher concentration of U-centers corresponds to higher values of T_c of the superconducting phase.

As it was mentioned above, the establishment of the equilibrium value of the resistance $R(t\to\infty)$ after the pressure removal occurs almost twice faster than under the action of pressure. This experimental fact is also explained within the framework of the proposed coalescence of oxygen clusters mechanism. Indeed, under the pressure application conditions, the process of filling clusters with oxygen ions by the accelerated "one-file" diffusion mechanism is realized only at the initial stage, and further, this process and the decrease in electrical resistance, is limited by the slower mechanism

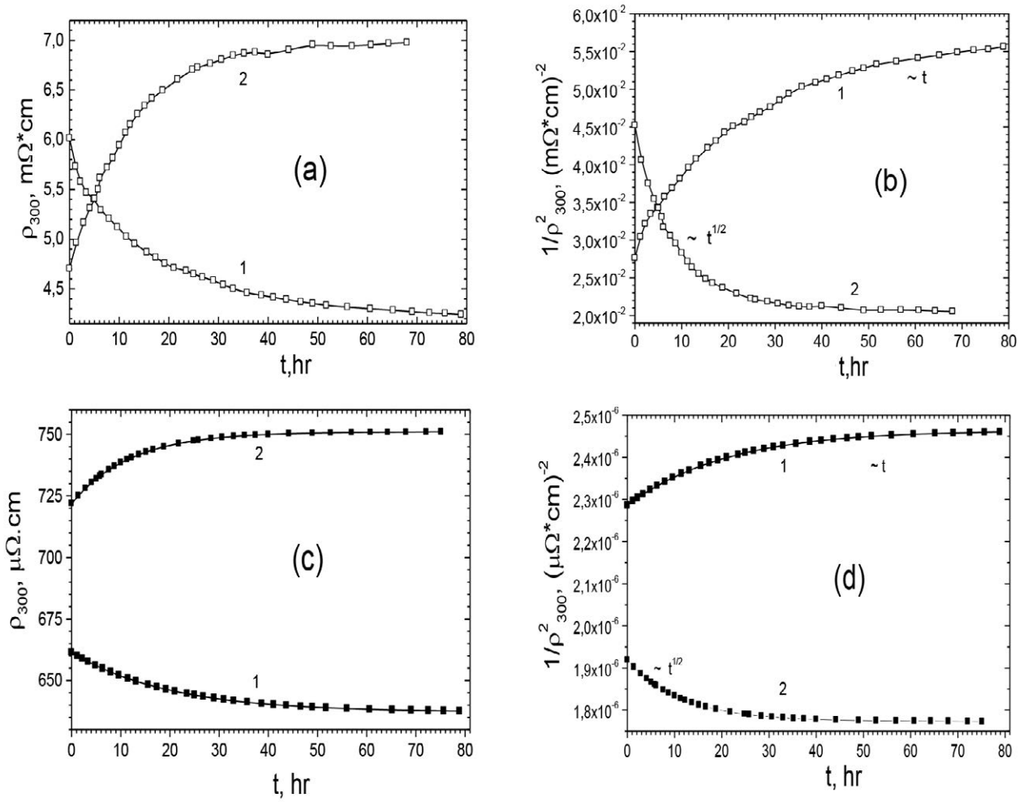

Fig.1. Time dependences of the electrical resistivity at room temperature in coordinates: ρ_{300} - t and $1/\rho^2_{300}$ – t for $YBa_2Cu_3O_{7-x}$ ((a) and (b)) and $HoBa_2Cu_3O_{7-x}$ ((c) and (d)) single crystals, measured immediately after application (curves 1) and removal (curves 2) of high hydrostatic pressure.

of classical diffusion. After the pressure removal the process of more intensive increase in the size of oxygen clusters is suspended. Herewith, as the time passes, the number of not fully completed clusters increases and there is a relaxation of the resistance. Under these conditions, the movement of oxygen ions is at much shorter distances and can be realized in the "one-file' diffusion regime, practically, until the equilibrium value $\rho(t\to\infty)$. A certain role in this may be played by the presence of structural and kinematic anisotropy in the system [32-37].

Notably, despite the higher Tc and the smaller oxygen deficiency, in the case of the $HoBa_2Cu_3O_{7-x}$ samples, all the characteristic changes in the form of the electrical resistivity temperature dependences and the absolute values of the resistive parameters that were observed during the pressure application-removal process at room temperatures were not less pronounced than for the $YBa_2Cu_3O_{7-x}$ samples. Apparently, in the case of $HoBa_2Cu_3O_{7-x}$, the substitution of yttrium by holmium which has a larger ionic radius, can play a role on the structural order in the system, which in turn leads to a change in the interaction of the oxygen ions in the CuO planes. Indeed, as is known from the literature [1,2,6,29], when yttrium is replaced by rare-earth elements with a larger ionic radius, significant qualitative changes occur in the $T_c(x)$ dependences. Therefore, the characteristic for the $YBa_2Cu_3O_{7-\delta}$ $T_c(x)$ dependence with two plateaus, at 60 and 90 K, degenerates into a much sharper monotonic dependence [1,2]. Thus, it can be assumed that in the case of deviation from oxygen stoichiometry, the $HoBa_2Cu_3O_{7-x}$ compound should be characterized by a much more disordered oxygen superstructure in comparison with the $YBa_2Cu_3O_{7-x}$.

Thus, we can conclude, that the external hydrostatic pressure P ≈ 5 kbar substantially intensifies the process of the diffusion coalescence of oxygen clusters, i.e., causes the growth of their average size. In turn, the increase in the size of oxygen clusters leads to an increase in the number of negative U-centers, the presence of which leads to the appearance of a phase capable of generating paired carriers of electric charge and, accordingly, characterized by a higher transition temperature T_c.

Acknowledgements

The work was partially supported by the European Union Horizon 2020 research and innovation program under Marie Sklodowska-Curie Grant Agreement No. 644348 (MagIC).

References

1. H. Lutgemeier, S. Schmenn, P. Meuffels, O. Storz, R. Schollhorn, Ch. Niedermayer, I. Heinmaa, Yu. Baikov, Physica C 267, 191-203 (1996).
2. R.V. Vovk, A.L. Solovyov, Low. Temp. Phys. 44, 81 (2018).
3. A. Driessen, R. Griessen, N. Koeman, E. Salomons, R. Brouwer, D.G. De Groot, K. Heeck, H. Hemmes, J. Rector, Phys. Rev. B 36, 5602 (1987).
4. A.L. Solovjov, L.V. Omelchenko, R.V. Vovk, O.V. Dobrovolskiy, Z.F. Nazyrov, S.N. Kamchatnaya, D.M. Sergeyev, Physica B 493, 58-67 (2016).
5. J.D. Jorgencen , P. Shiyou, P. Lightfoot, H. Shi, A.P. Paulikas, B.M.W. Veal, Physica C 167, 571 (1990).
6. R. V. Vovk, N. R. Vovk, O. V. Dobrovolskiy / Journal of Low Temperature Physics (2014) PP. 1 - 17 DOI 10.1007/s10909-014-1121-9.
7. B. Martinez, F. Sandiumenge, S. Pinol, N. Vilalta, J. Fontcuberta, X. Obradors, App. Phys. Lett. 66, 772–774 (1995).
8. R. V. Vovk, N. R. Vovk, I. L. Goulatis, A. Chroneos / Journal of Low Temperature Physics (2014) 174: p.p. 214-221 DOI:10.1007/s10909-013-0959-6.
9. D.A. Lotnyk, R.V. Vovk, M.A. Obolenskii, A.A. Zavgorodniy, J. Kováč, M. Kaňuchová, M. Šefciková, V. Antal, P. Diko, A. Feher, A. Chroneos, J. Low Temp. Phys. 161, 387-394, (2010).
10. R. Menegotto Costa , F.T. Dias , P. Pureu, X. Obradors, Physica C 495, 202–207 (2013).
11. G.Y. Khadzhai, R.V. Vovk, N.R. Vovk, S.N. Kamchatnaya, O.V. Dobrovolskiy, Physica C 545, 14-17 (2018).
12. H.A. Borges, M.A. Continentino, Solid State Commun. 80, 197 (1991).
13. R.V. Vovk, M.A. Obolenskii, A.A. Zavgorodniy, I.L. Goulatis, A.I. Chroneos. J. Mater. Sci.: Mater. Electron. 22, 20-24 (2011).
14. M. Sarikaya, R. Kikuchi, I.A. Akhay, Physica C 152, 161-170 (1988).
15. A.V. Bondarenko, A.A. Prodan, M.A. Obolenskii, R.V. Vovk, T.R. Arouri, Low Temp. Phys. 27, 339-344 (2001).
16. R.V. Vovk, Z.F. Nazyrov, M.A. Obolenskii, I.L. Goulatis, A. Chroneos, V.M. Pinto Simoes, J. Alloys Compd. 509, 4553–4556 (2011).
17. K. Widder, A. Zibold, M. Merz, H.P. Geserich, A. Erb, G. Müller-Vogt, Physica C 232, 82-88 (1994).
18. R.V. Vovk, N.R. Vovk, G.Ya. Khadzhai, I.L. Goulatis, A. Chroneos, Physica B 422, 33–35 (2013).
19. O.V. Dobrovolskiy, M. Huth, V.A. Shklovskij, R.V. Vovk, Sci. Rep. 7, 13740 (2017).
20. O.V. Dobrovolskiy, R. Sachser, M. Huth, V.A. Shklovskij, R.V. Vovk, V.M. Bevz, M. Tsindlekht. Appl. Phys. Lett. 112, 152601 (2018).
21. A.L. Solovyov, L.V. Omelchenko, V.B. Stepanov, R.V. Vovk, H.U. Habermeier, P. Przyslupski, K. Rogacki, Phys. Rev. B 94, 224505 (2016).
22. L. Mendonca Ferreira at al. Phys. Rev. B 69, 212505 (2004).
23. R.V. Vovk, N.R. Vovk, G.Ya. Khadzhai, I.L. Goulatis, A. Chroneos, Physica B 422, 33–35 (2013).
24. J. Ashkenazi, J. Supercond. Nov. Magn. 24, 1281 (2011).
25. R. Griessen, Phys. Rev. B 36, 5284 (1987).
26. R.V. Vovk, N.R. Vovk, G.Ya. Khadzhai, O.V. Dobrovolskiy, Z.F. Nazyrov, Curr. Appl. Phys. 14, 1779-1782 (2014).
27. R.V. Vovk, N.R. Vovk, G.Ya. Khadzhai, O.V. Dobrovolskiy, Solid State Commun. 204, 64-66 (2015).
28. P. Schleger et al. Physica C 176, 261-273 (1991).
29. R. V.Vovk et al. J. Alloys Compd. 453, 69-74 (2008).
30. Yu.I. Boiko, V.V. Bogdanov, R.V. Vovk, S.N. Kamchatnaya, I.L. Goulatis, A. Chroneos. Mater. Res. Express 4, 096001 (2017).
31. K. Mitsen, O. Ivanenko Physica C 408-410, 422-423 (2004).
32. C.A. Downing, M.E. Portnoi, Nature Commun. 8, 897 (2017).
33. R.V. Vovk, G.Ya. Khadzhai, O.V. Dobrovolskiy, Appl. Phys. A 117, 997-1002 (2014).
34. P.G. Curran, V.V. Khotkevych, S.J. Bending, A.S. Gibbs, S.L. Lee, A.P. Mackenzie, Phys. Rev. B 84, 104507 (2011).
35. R.V. Vovk, N.R. Vovk, G.Ya. Khadzhai, I.L. Goulatis, A. Chroneos, Solid State Commun. 190, 18-22 (2014).
36. I.N. Adamenko, K.E. Nemchenko,V.I. Tsyganok, A.I. Chervanev, Low Temp. Phys. 20, 498 (1994).
37. R.V. Vovk, M.A. Obolenskii, A.A. Zavgorodniy, I.L. Goulatis, A. Chroneos, E.V. Biletskiy, J. Alloys Compd. 485, 121-123 (2009).

Section: Physics seminar

Microwave-stimulated superconductivity in the vortex state

V. M. Bevz, R. V. Vovk, V. A. Shklovskij, A.I. Bezuglyj, O.V. Dobrovolskiy

V.N. Karazin Kharkov National University, Svoboda Sq. 4, Kharkov, Ukraine, 61022
dobrovolskiy@physik.uni-frankfurt.de

In the mixed state of type-II superconductors penetrated by an external magnetic field in the form of a lattice of Abrikosov vortices, the dc resistance is known to increase with increasing velocity of the vortex lattice [1]. Accordingly, vortex pinning sites impeding the vortex motion are widely used to preserve the low-dissipative response of the system [2]. In our recent experiments we subjected superconducting Nb films with nanogrooves to a high-frequency ac current stimulus [3-5]. By tuning the number of mobile and pinned vortices by varying the magnetic field around the so-called matching values, Fig. 1, we observe a completely opposite effect [6]. Namely, the vortex-related microwave excess loss for mobile vortices becomes smaller than for pinned vortices in a certain range of power levels at ac current frequencies above 100 MHz. This is distinct from the well-known phenomenon of microwave-stimulated superconductivity in the Meissner state [7, 8]. Thus, our findings appeal for the development of a theory of microwave-stimulated superconductivity in the vortex state. Generalization of the theory is currently under way and the theoretical results soon will be presented in comparison with the experimental data.[1] E. H. Brandt, Rep. Progr. Phys. 58 (1995) 1465.

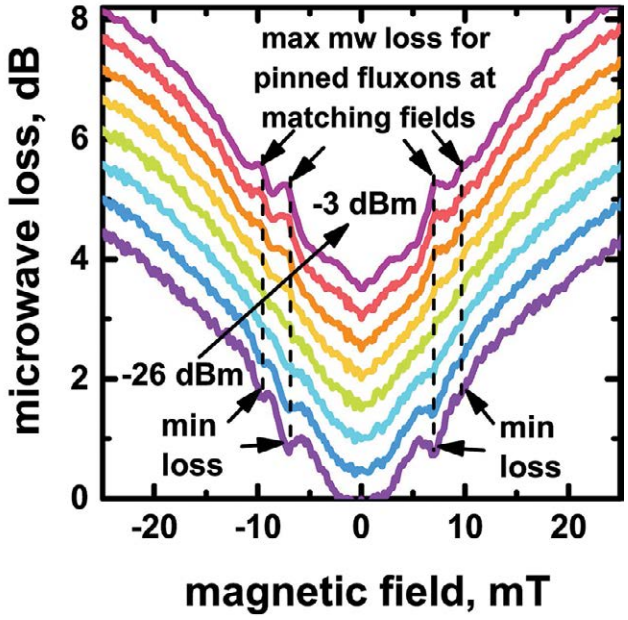

Fig. 1. Vortex-related microwave losses as a function of the magnetic field value for a series of microwave power levels, as indicated. While at lower ac power levels, the microwave loss is minimal at the so-called matching values *(7.2 mT and 9.6 mT)*, when the vortex lattice is commensurate with the periodic pinning nanostructure, at high power levels the minima turn into maxima indicating that pinned vortices dissipate less than the mobile ones.

References

1. E. H. Brandt, Rep. Progr. Phys. 58 (1995) 1465.
2. O. V. Dobrovolskiy, Physica C 533 (2017) 80.
3. O.V. Dobrovolskiy and M. Huth, Appl. Phys. Lett. 106 (2015) 142601.
4. O.V. Dobrovolskiy, M. Huth, V. A. Shklovskij, Appl. Phys. Lett. 107 (2015) 162603.
5. O. V. Dobrovolskiy et al., Scientific Reports 7 (2017) 13740.
6. O. V. Dobrovolskiy et al., Phys. Status Solidi RRL (2018), 1800223.
7. A. F. G. Wyatt et al., Phys. Rev. Lett. 16 (1966), 1166.
8. I. V. Zolochevskii, Low Temp. Phys. 39 (2013) 571.

https://doi.org/

ІНФОРМАЦІЯ ДЛЯ АВТОРІВ СТАТЕЙ

журналу «Вісник ХНУ». Серія «Фізика»

У журналі «Вісник ХНУ». Серія «Фізика» друкуються статті та стислі за змістом повідомлення, в яких наведені оригінальні результати теоретичних та експериментальних досліджень, а також аналітичні огляди літературних джерел з різноманітних актуальних проблем фізики за тематикою видання.

Мова статей – українська, англійська та російська.

ТЕМАТИКА ЖУРНАЛУ

1. Теоретична фізика.
2. Фізика твердого тіла.
3. Фізика низьких температур.
4. Фізика магнітних явищ.
5. Оптика та спектроскопія.
6. Загальні питання фізики і серед них: методологія та історія фізики, математичні методи фізичних досліджень, методика викладання фізики у вищій школі, техніка та методика фізичного експерименту тощо.

ВИМОГИ ДО ОФОРМЛЕННЯ РУКОПИСІВ СТАТТЕЙ

Загальний обсяг тексту рукопису статті повинен займати не більше, ніж 15 сторінок.

Рукопис статті складається з титульної сторінки, на якій вказанно: назва статті; ініціали та прізвища авторів; поштова адреса установи, в якій була виконана робота; класифікаційний індекс за системами PACS та УДК; анотації на окремому аркуші з прізвищем та ініціалами авторів і назвою статті, викладені українською, російською та англійською мовами; основний текст статті; список літератури; підписи під рисунками; таблиці; рисунки: графіки, фотознімки.

Анотація повинна бути за об'ємом не меньш ніж 500 символів. Стаття повинна бути структорована. Висновки потрібно пронумеровати та в них потрібні бути висновки а не переписана анотація.

Електронний варіант рукопису статті повинен відповідати таким вимогам: текст рукопису статті повинен бути набраний у форматі MicrosoftWord версії 2013, вирівнювання тексту повинне бути здійснене за лівим краєм, гарнітураTimesNewRoman, без прописних букв у назвах, букви звичайні рядкові, з полями ліворуч, праворуч, зверху і знизу по 2,5 см, формули повинні бути набрані в MathType (не нижче версії 6,5), у формулах кирилиця не допускається, символи з нижніми і верхніми індексами слід набирати в MicrosoftWord, ширина формули не більше 70 мм, графіки та фотографії необхідно подавати в графічному форматі, розрізнення не менше 300 dpi, поширення файлів повинно бути *.jpg, шириною в одну чи дві колонки, для однієї колонки розміри: завширшки 8 мм, для двох колонок – 16 мм. Масштаб на мікрофотографіях необхідно представляти у вигляді масштабної лінійки.

ВИМОГИ ДО ОФОРМЛЕННЯ ГРАФІКІВ

Товщина ліній не більше 0,5 мм, але не менше 0,18 мм. Величина літер на підписах до рисунків не більш 14 pt , але не менше 10 pt, гарнітура Arial.

ПРИКЛАД ОФОРМЛЕННЯ СПИСКУ ЛІТЕРАТУРИ

1. Л.Д. Ландау, Е.М. Лифшиц. Теория упругости, Наука, М. (1978), 730 с.
2. И.И. Іванов. ФТТ, 25, 7, 762 (1998).
3. A.D. Ashby. Phys.Rev., A19, 213 (1985).
4. D.V. Vert. In Progress in Metals, ed. by R. Speer, USA, New York (1976), v.4, p.17.

ДО РЕДАКЦІЇ НАДАЄТЬСЯ

1. Два роздруковані примірники рукопису статті, які підписані її авторами.
2. Електронна версія рукопису та дані щодо контактів для спілкування з її авторами. Для цього потрібно надіслати електронною поштою, тільки на адресу physics.journal@karazin.ua.
3. Направлення від установи, де була виконана робота, і акти експертизи у двох примірниках; адресу, прізвище, повне ім’я та батькові авторів; номери телефонів, E-mail, а також зазначити автора рукопису, відповідального за спілкування з редакцією журналу.

Матеріали рукопису статті потрібно направляти за адресою: Редакція журналу «Вісник Харківського національного університету імені В.Н. Каразіна. Серія: фізика», Лебедєву С.В., фізичний факультет, майдан Свободи, 4, Харківський національний університет імені В.Н. Каразіна. тел. (057)-707-53-83.

Наукове видання

Вісник Харківського національного університету імені В.Н.Каразіна

Серія “Фізика”

випуск 23

Збірник наукових праць

Українською, російською та англійською мовами.

Комп’ютерне верстання С.В. Лебедєв

Підписано до друку 28.12.2016. Формат 60х84 1/8.

Папір офсетний. Друк ризограф. Ум. друк. арк. 11,9. Обл.-вид. арк 18,7.

Наклад 100 пр. Зам. №

Надруковано: ХНУ імені В.Н. Каразіна

61022, Харків, майдан Свободи, 4.
Тел.705-24-32

Свідоцтво суб'єкта видавничої справи ДК №3367 від 13.01.09